Title	Experimental study on direct-drive inertial confinement fusion with diamond material targets
Author(s)	川﨑, 昂輝
Citation	大阪大学, 2024, 博士論文
Version Type	VoR
URL	https://doi.org/10.18910/96081
rights	
Note	

Doctoral Dissertation

Experimental study on direct-drive inertial confinement fusion with diamond material targets

ダイヤモンド材料ターゲットを用いた直接駆動慣性閉じ込め核融合に関する研究

KAWASAKI Koki

December 2023

Graduate School of Engineering,
Osaka University

Abstract

This dissertation explored developing and characterizing diamond capsules and laser-plasma interactions (LPIs) for direct-drive inertial confinement fusion (ICF).

In the first chapter, the principles and overview of nuclear fusion are explained, and the aim of the dissertation is introduced. Nuclear fusion is a promising energy source in the future thanks to advantages such as not emitting greenhouse gases. ICF is one of the approaches to confine fusion plasmas, and adjustable power production is attractive. This study was performed to contribute to improving the performance of ICF.

The second chapter explains the physics/issues of ICF and this study's background. Achieving a high gain ignition is necessary to obtain inertial fusion energy (IFE), which is industrial power produced in a plant. To realize it, a tiny capsule that contains fusion fuels (1-3 mm in diameter) is compressed by high-power lasers $I \sim 10^{15}$ W/cm^2 in direct-drive ICF. However, ablation surface perturbations called laser imprinting due to non-uniform laser irradiation, and the growth of such perturbations by Rayleigh Taylor (RT) instability is detrimental issues. To address these issues, target-based approaches such as a foam target, high Z coating, and a diamond target were explored, and advanced schemes such as fast ignition (FI) and shock ignition (SI) schemes were proposed. This study focused on diamond targets which can mitigate laser imprinting. Also, it should be noted that diamond targets can be applied to advanced schemes such as SI scheme. This study explored the fabrication of diamond capsules and LPIs in diamond targets to provide fundamental technologies of capsule fabrication and an essential understanding of LPIs to apply diamond targets to direct-drive ICF. It should also be noted that understanding LPIs and subsequent hot electron (HE) generation is very important in SI scheme where a high intensity laser pulse is employed.

The third chapter shows the study for the development and characterization of diamond capsules. Diamond can mitigate laser imprinting thanks to its low compressibility and higher density than conventional plastic targets. In this study, diamond was deposited by hot-filament chemical vapor deposition (HF-CVD) technique, which is advantageous for mass production compared to microwave plasma chemical vapor deposition (MP-CVD) employed in previous works. Firstly, the deposition conditions were optimized, and the fabrication process was improved from the previous works. Next, the fabricated diamond capsules were comprehensively characterized. As a result, diamond capsules with surface uniformity of several 10 nm were obtained, and essential parameters for the capsule, such as non-diamond contents, thickness, density, and mode amplitude, were revealed. Then,

the characterized diamond capsules were introduced to a laser irradiation experiment, and the implosion trajectories were observed by X-ray diagnostics. As a result, successful implosion was observed, and their trajectories were consistent with radiation hydrodynamic simulation calculations, verifying the quality of diamond capsules and the accurate characterization. These results showed that diamond capsules can be fabricated in the process that applies to mass production.

In the fourth chapter, the studies for LPIs and HEs are shown. In high-intensity laser irradiation, stimulated Raman scattering (SRS) and two plasmon decay (TPD) occur, and they produce Langmuir waves (LWs) that lead to HE generation. HEs could be either detrimental or beneficial in direct-drive ICF. It is known that the growth rates of these instabilities in inhomogeneous plasmas are depicted by Rosenbluth gain. However, LWs could damp through various mechanics, and therefore, the extent of SRS, TPD, and HEs is not apparent, which needs experimental investigation. To explore LPIs in diamond target, an experimental platform that enables characterization for SRS, TPD, and HEs was developed at the GEKKO-XII laser facility, and the extent of SRS/TPD and conversion ratio of HEs were revealed in a conventional plastic target. Then, SRS, TPD, and HEs in diamond targets were explored and compared with plastic. It was found that SRS, TPD, and HEs decreased in diamond which did not contain hydrogen (H) in the material. From the analysis, the difference between diamond and plastic was attributed to high ion wave damping due to H ions. These results suggested that low H concentration is advantageous in suppressing HE generation while HEs could be controlled by tuning H concentration in target materials when active control of HEs is important. In this respect, the design of diamond capsules for direct-drive ICF application is discussed.

In the fifth chapter, the conclusion of this dissertation is given.

Acknowledgment

Firstly, I would like to thank my supervisor, Professor Keisuke Shigemori, for giving me many special opportunities and supporting me for five years of study. I would like to thank Professor Isao Murata and Associate Professor Eiji Hoashi at the Graduate School of Engineering, Osaka University, for precious comments for the dissertation. I would like to thank Associate Professor Yoichiro Hironaka (Current affiliation: Ex-Fusion Inc.), Kohei Yamanoi, and Hideo Nagatomo at the Institute of Laser Engineering (ILE), Osaka University for helping me with experiments, simulations, and discussion. I would like to thank the team leader of a diamond team at the National Institute of Advanced Industrial Science and Technology (AIST), Hideaki Yamada, for his help with deposition experiments and supporting a study at AIST. I would also like to thank diamond team members Dr. Akiyoshi Chayamaha, Dr. Yoshiaki Mokuno, and Dr. Takehiro Shimaoka for their help in deposition experiments. I would like to thank Dr. Gabriele Cristoforetti from the Intense Laser Irradiation Laboratory, INO-CNR, Italy, for helping me analyze experimental data in the GEKKO experiment. I would like to thank Professor Ryosuke Kodama, Associate Professor Norimasa Ozaki, Dr. Kento Katagiri, and students at Kodama Lab. in the Graduate School of Engineering, Osaka University, for the help of experiments to obtain data from a streaked optical pyrometer. I would like to thank Professor Shinsuke Fujioka and Mr. Ryunosuke Takizawa at ILE for their help in experiments to get X-ray spectrometer data. I would like to thank Professor Masahiro Tsukamoto and associate Professor Yuji Sato at Joining and Welding Research Institute, Osaka University, for help with Raman spectroscopy. I would like to thank the technical staff at ILE for operating the GEKKO-XII laser and fabricating experimental targets. Also, I would like to thank the technical staff at AIST for helping my experiment. I am grateful to group members Mr. Toshinori Iwasaki, Mr. Yuto Maeda, Mr. Daisuke Tanaka, Mr. Takumi Tamagawa, Mr. Tomoyuki Idesaka, Mr. Chiharu Nakatsuji, and Mr. Sota Matsuura for helping me with experiments and various staffs. Finally, I want to thank my parents for always supporting me.

This study was performed under the NIFS Collaboration Research program (No. 2021NIFS20KUGK127, 2021NIFS21KUGK136), and this study was supported by the Japan Society for Promotion of Science, KAKENHI (Grant No. 17H02996 and JP22J22774), and partially supported by a grant from the MEXT Quantum Leap Flagship Program No. JPMXS0118067246.

This dissertation is based on the articles below. The permission to reuse and reproduce the contents in the articles are given by each publisher (AIP publishing, Elsevier, and

APS).

- K. Kawasaki, Y. Hironaka, Y. Maeda, T. Iwasaki, D. Tanaka, K. Miyanishi, H. Nagatomo, S. Fujioka, N. Ozaki, R. Kodama, T. Matsuoka, D. Batani, J. Trela, P. Nicolai, and K. Shigemori, *The role of hot electrons on ultrahigh pressure generation relevant to shock ignition conditions*, High Energy Density Physics 37, 100892 (2020), https://doi.org/10.1016/j.hedp.2020.100892, Copyright Elsevier (2020).
- K. Kawasaki, D. Tanaka, H. Yamada, S. Ohmagari, Y. Mokuno, A. Chayahara, T. Tamagawa, Y. Hironaka, K. Yamanoi, M. Tsukamoto, Y. Sato, T. Somekawa, H. Nagatomo, K. Mima, and K. Shigemori, *Direct-drive implosion experiment of diamond capsules fabricated with hot filament chemical vapor deposition technique*, Physics of Plasmas 28, 104501 (2021), https://doi.org/10.1063/5.0065430, Copyright AIP publishing (2021).
- K. Kawasaki, H. Yamada, H. Nagatomo, Y. Hironaka, K. Yamanoi, D. Tanaka, T. Idesaka, Y. Mokuno, A. Chayahara, T. Shimaoka, K. Mima, T. Somekawa, M. Tsukamoto, Y. Sato, A. Iwamoto, and K. Shigemori, *Fabrication of nanocrystalline diamond capsules by hot-filament chemical vapor deposition for direct-drive inertial confinement fusion experiments*, Diamond and Related Materials 135, 109896 (2023), https://doi.org/10.1016/j.diamond.2023.109896, Copyright Elsevier (2023).
- K. Kawasaki, G. Cristoforetti, T. Idesaka, Y. Hironaka, D. Tanaka, D. Batani, S. Fujioka, LA. Gizzi, M. Hata, T. Johzaki, K. Katagiri, R. Kodama, S. Matsuo, H. Nagatomo, Ph. Nicolai, N. Ozaki, Y. Sentoku, R. Takizawa, A. Yogo, H. Yamada, and K. Shigemori, *Effects of Hydrogen Concentration in Ablator Material on Stimulated Raman Scattering, Two Plasmon Decay and Hot Electrons for Direct-Drive Inertial Confinement Fusion*, Physical Review Research 5, 033051 (2023), https://doi.org/10.1103/PhysRevResearch.5.033051, Copyright APS (2023)

Table of Contents

List of Figures

List of Table

1. Introduction and research background

1.1. Principle of nuclear fusion

In a fusion reaction, two or more light nuclei are combined into one or more heavier nuclei. At the reaction, mass-energy is released according to Einstein's mass-energy relationship [1].

$$Q = \left(\sum_i m_i - \sum_f m_f \right) c^2 \tag{1.1}$$

Here, m and c indicate the mass of nuclei and the speed of light, and i and f denote the initial and final products, respectively. For example, in the DT reaction, deuterium (D) and tritium (T) fuse into an alpha particle (helium nucleus) and a neutron, releasing a mass-energy of $Q = 17.6$ MeV. Based on the momentum conservation, produced energy is distributed to an alpha particle with 3.6 MeV and a neutron with 14.1 MeV, respectively.

$$\mathrm{D} + \mathrm{T} \rightarrow \alpha\ (3.6\ \mathrm{MeV}) + \mathrm{n}(14.1\ \mathrm{MeV}) \tag{1.2}$$

These values are significantly larger than those of chemical reactions; for example, it is around one million larger than that of the ionization energy of hydrogen 13.6 eV.

Two positively charged nuclei must come into contact to fuse, overcoming the repulsive Coulomb force. Cross-section, defined as the probability of a fusion reaction, can be calculated by Quantum mechanics. In the DT reaction, it peaks at a center-of-mass kinetic energy of around 60 keV, indicating that fusion reactions require extremely high-energy particles. Fig 1.1 shows plots of cross-sections for some famous reactions [2]. DT reaction has the largest cross-section in this energy range, making it the most attractive to achieve controlled nuclear fusion.

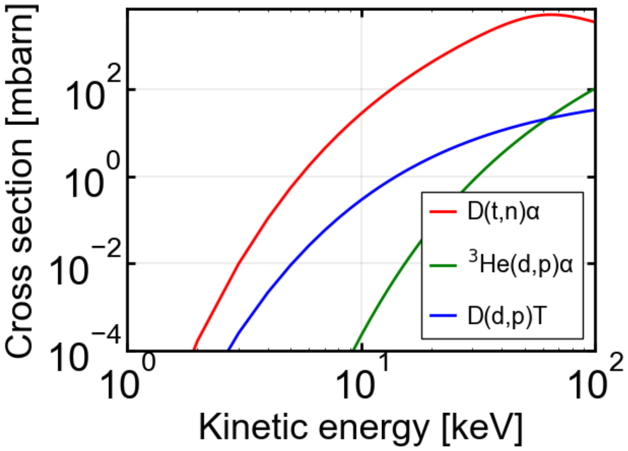

Figure 1.1. Cross-sections of famous fusion reactions as a function of a center-of-mass kinetic energy. D, T, n, α, and p indicate deuterium, tritium, neutron, alpha particle, and proton.

1.2. Approaches of nuclear fusion

One way to cause fusion reactions is to accelerate D nuclei up to high energy and shoot it onto the T target. However, the cross-section for Coulomb scattering is much larger than that of fusion reactions, which means that most beam particles lose their energy before fusion reactions. A more practical method is to make a DT plasma of sufficiently high temperature. In thermal equilibrium, the Coulomb collisions redistribute the kinetic energy in a plasma, and fusion reactions will occur eventually after a sequence of collisions. This approach is called thermonuclear fusion. [1]. It is required to keep sufficiently hot plasma together over a sufficient time at a certain density. The required temperature is calculated when the internal heating by fusion products W_{in} exceeds all energy loss W_{out}. The power produced from fusion reactions per unit volume is calculated by

$$W_{fus} = \frac{1}{4} n^2 \langle \sigma v \rangle Q_{DT} \tag{1.3}$$

Here, n is the density of a DT plasma in $n_D = n_T = n/2$, $\langle \sigma v \rangle$ is a reactivity defined as a probability of reactions per unit time and unit density, and Q_{DT} is a power produced from a single DT reaction. Since alpha particle mainly contributes to plasma heating, W_{in} equals $W_{fus}/5$. For energy loss, radiative loss by bremsstrahlung is a dominant mechanism: $W_{out} \sim W_{rad}$. Here, W_{rad} is described by

$$W_{rad} \propto n_e^2 T^{\frac{1}{2}} \tag{1.4}$$

Where n_e is a plasma electron density in $n_i = n_e = n$, and T is an electron temperature. Fig. 1.2. shows values of W_{in}/n^2 and W_{out}/n^2 as a function of temperature. A minimum temperature for keeping fusion reactions can be calculated by $W_{in} = W_{out}$, obtaining around 5 keV [1]. Typically, a temperature of ~ 10 keV is regarded as an ideal value.

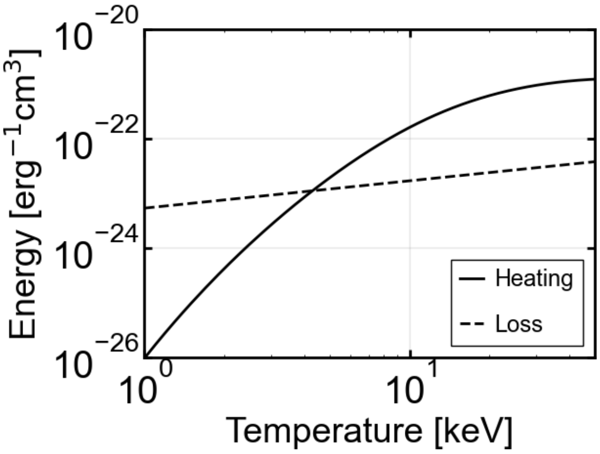

Figure 1.2. Energy deposition and energy dissipation in a fusion plasma as a function of temperature.

In such high temperatures, any structural material melts, and therefore, a confinement method must be devised. There are two main approaches: magnetic confinement fusion (MCF) and inertial confinement fusion (ICF) [1]. In MCF, plasma particles are trapped by a magnetic field. In this approach, the pressure of a plasma cannot be larger than the magnetic field pressure, limiting a plasma density low. It requires keeping plasma confined for some duration to achieve sufficient energy production. In ICF, which is the main theme of this dissertation, a fuel capsule is compressed into ultra-high density by energy drivers, which is called implosion, and the adiabatically heated plasma at peak compression is confined by its inertia until it explodes for a very short time [3].

1.3. Aim of this study

Fossil fuel power generation is currently a primary approach for terrestrial power production. However, it emits greenhouse gases such as carbon dioxide that cause global warming, and those fossil fuels would be exhausted in several decades. Nuclear fusion is attractive for future power generation [4]. It can produce large amounts of energy and does not emit greenhouse gases. Also, DT fuels are unexhausted because D is procured from water, and T can be created by injecting neutrons into lithium, which is plentiful on the Earth. Moreover, runaway reactions are never expected, which is a severe problem of nuclear fission power generation. ICF is called laser fusion when lasers are employed as energy drivers. Laser fusion is advantageous because power production can be easily controlled by changing the repetition rate of laser irradiation. This dissertation aims to contribute to the improvement of laser fusion. In the following manuscript, laser fusion is called ICF because it is the most general and widely recognized term.

2. Basics of Inertial confinement fusion and role of this dissertation

2.1. Target gain

In ICF, as a result of implosion, it is expected that more energy E_f is produced from fusion reactions than laser energy E_l. Target gain is defined by $G = E_f/E_l$. The term "ignition" is used for $G > 1$. It was achieved at LLNL in 2022 [5–7], which is mentioned later. For inertial fusion energy (IFE), which is a term to describe industrial energy production by ICF, ignition is not a goal. ICF power plant will operate based on an energy cycle as shown in Fig. 2.1 [1].

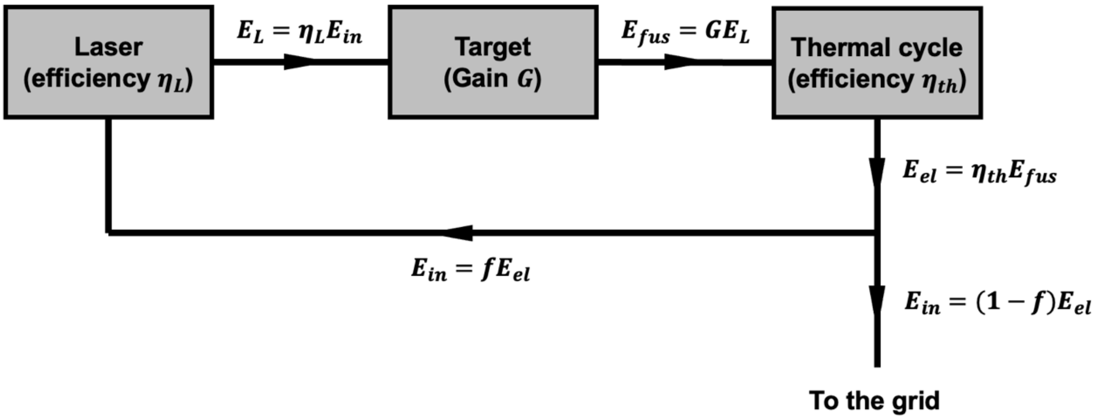

Figure 2.1. Energy cycle in ICF power plant.

In the system, the energy produced by fusion reactions E_{fus} is converted into electricity E_{el} by thermal cycle with an efficiency η_{th}. A fraction f of electricity is used to operate laser E_{in}, and the remaining $(1-f)$ is sent to the grid. In a laser facility, electricity E_{in} is converted to laser energy E_L with an efficiency η_L, and E_{fus} is produced by fusion reactions with a target gain G. The energy balance for this cycle is written by

$$f\eta_L\eta_{th}G = 1 \tag{2.1}$$

By inserting the values of f, η_L, η_{th}, the value G required for IFE can be calculated. Usually, $G\sim100$ is required in practical operation [1].

2.2. Target design

In ICF, DT fuels are held by a spherical capsule, and the capsule absorbs laser energy, and ablation pressure drives implosion. In this respect, a capsule is often called an ablator. In general, ablator materials should consist of low atomic number (Z) elements to minimize bremsstrahlung emissions that are regarded as energy loss and cause of fuel preheating. It is known that a target gain decreases with increasing preheating [1]. Plastic has been the most typical low-Z ablator material [8].

The mass of DT fuels should be small because the energy from a single explosion must be limited to a few GJ to avoid damage in an ICF power plant vessel. The mass of spherical DT fuels with radius R and density ρ is described by

$$M = 4\pi\rho R^3/3 = 4\pi(\rho R)^3/3\,\rho^2 \tag{2.2}$$

With a constant value of ρR, compression (i.e., a large value of ρ) is required to obtain a small mass. The value of ρR is determined in terms of burn efficiency $\phi = N_{fus}/N_{DT}$ where N_{fus} and N_{DT} are the number of fusion reactions and DT pairs initially present in the plasma. It is known that ϕ is an increased function of ρR, and $\rho R \sim 3$ g/cm^3 is required to achieve an adequate burn efficiency (~0.3) for a high target gain. Without compression, solid DT 0.2 g/cm^3 needs ~ 3 kg to obtain $\rho R \sim 3$ g/cm^3 according to Eq. (2.2). 3 kg DT fuels produce 300 TJ based on $17.6\ \mathrm{MeV}/2m_{DT} = 337\ \mathrm{GJ/g}$ with a burn fraction ~0.3, which is unrealistically large. When solid DT is, for example, compressed by 1000 times, ρR of ~ 3 can be achieved at a mass ~3 mg, which produces a controllable amount of fusion energy ~300 MJ [9,10].

DT fuels usually consist of two layers (cryogenic and gas layers) as shown in Fig. 2.2. Necessity of this two-layered structure can be explained by estimating a target gain assuming whole DT fuels are heated up to ultrahigh temperature ~5 keV.

$$G = \frac{E_{fusion}}{E_{thermal}} \phi \eta \tag{2.3}$$

Here, E_{fusion} and $E_{thermal}$ are energy from fusion reactions and thermal energy of DT plasma per unit mass, and η is a beam to fuel coupling ratio. When assuming practical values ($\phi = 0.3, \eta = 0.1$), the achievable maximum gain is calculated to be around 20 [1], which is insufficient for IFE. Therefore, heating only a small part to initiate fusion reactions was suggested. As a result of implosion, the DT ice layer becomes ultrahigh-density fuels, and the DT gas layer forms low-density ultrahigh temperature fuels called hot spot, as shown in Fig. 2.2. In the hot spot, fusion reactions start to occur, and burn waves propagate into the cold high-density part. The required hot spot size is estimated by considering the conditions that a major fraction of α particles can deposit their energy within the hot spot, and this typically requires $\rho_h R_h$ ~ 0.3 g/cm^2 where $\rho_h R_h$ is an arial density of hot spot [1]. This is a very small portion of DT fuels: only 10 % in areal density.

From the above, ICF capsules consist of a low Z ablator, DT ice and gas layers, and their mass is an order of mg. The detailed design of the thickness of an ablator, the total mass of DT fuels, and the ratio of ice and gas layer varies in several implosion designs. Typical capsule size is 1 to 3 mm in diameter [11]. For experimental purposes, a capsule of a smaller diameter, such as 0.5 mm, is also sometimes employed [12].

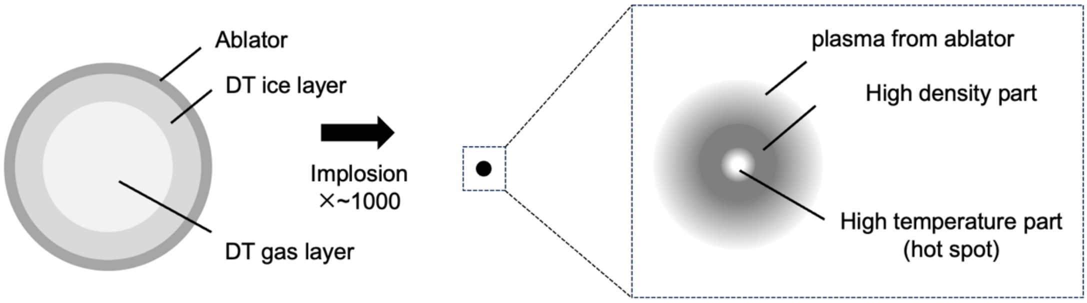

Figure 2.2. Schematics of typical target design and burning fuels at peak compression.

2.3. Implosion process

Once a laser hits a capsule, the capsule surface turns into a plasma, and the laser energy is absorbed in a low-density plasma up to a critical density point where a plasma frequency equals a laser frequency: $n_c = m_e \omega_L^2/(4\pi e^2) = 1.1 \times 10^{21}/\lambda_{L(\mu m)}^2$ [cm^{-3}], and absorbed energy is transported to the ablation surface. As a result, a reacting force, called ablation pressure, creates a shock wave inward. A shock wave is a discontinuous wave where parameters such as a density and a temperature drastically change before and after its propagation [13], and its propagation leads to the creation of an ultrahigh temperature hot spot surrounded by cold ultrahigh density fuels. The implosion of a fuel capsule is divided into four stages, as shown in Fig. 2.3 [11].

In early times, laser irradiation typically starts with one to three low-intensity pulses to generate several shock waves that propagate into the target. An entropy jump across a strong shock is proportional to $\Delta p/\rho^{5/3}$, where Δp is a pressure jump, and ρ is the pre-shock density, and therefore, a gradual compression is favored to minimize an entropy rise. The laser pulse intensity then increases, launching a stronger shock that merges with the earlier shocks. When the shock reaches the inner surface of the DT ice layer, a rarefaction wave moves outward toward the ablation surface, and the target shell and ice layer (typically collectively called the shell) begin to accelerate inward toward the target center. In the acceleration phase, the laser intensity increases, and a fuel capsule is imploded very fast, typically at around 300 km/s, while the main shock within the DT gas converges toward the target center. When the main shock wave reflects from the target center and returns to the converging shell, the deceleration phase begins. As the shell decelerates, its kinetic energy is converted into thermal energy and the DT fuels are compressed and heated. The attainable maximum temperature depends on the kinetic energy of the shell. In the final stage, peak compression occurs, and fusion reactions start in a central hot spot. Then, the heating by α particles propagates into surrounded cold fuels to burn a substantial part of DT fuel, as described in the previous section.

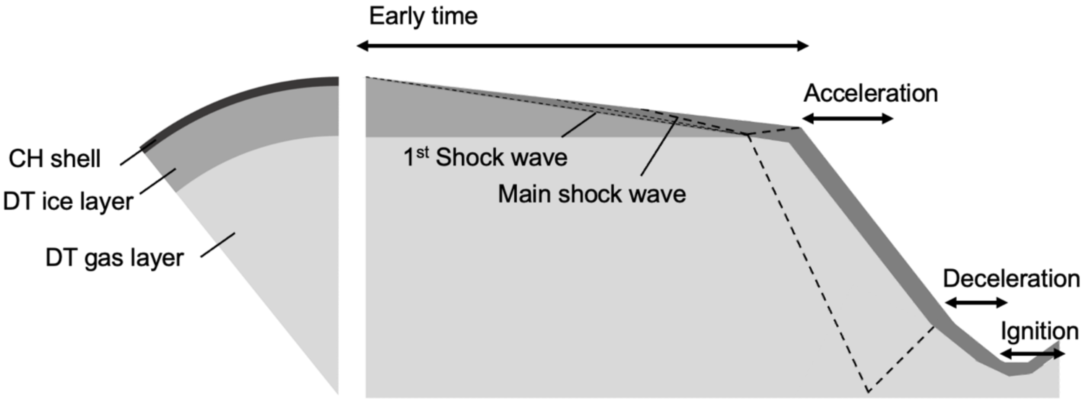

Figure 2.3. Implosion process in ICF.

2.4. Laser requirements

To implode the target at adequate implosion velocity, such as ~300 km/s, large ablation pressure, such as ~10 TPa, is typically required [10]. Here, an estimation of laser intensity required to achieve such high pressure is shown. When assuming that laser energy is absorbed at a critical density point via collisional absorption (inverse-bremsstrahlung), the thermal flux toward the ablation surface can be described by

$$I = f n_c m_e v_e^3 \tag{2.4}$$

Where I, f, n_c, m_e, and v_e are an absorbed laser intensity, a flux limiter coefficient, a critical density, the electron mass density, and an electron thermal velocity, respectively. Here, $(3/4)I = f n_c m_e v_e^3$ should be accurate because the absorbed energy is also transported to lower-density plasma, but here coefficient $3/4$ was ignored for the simplest discussion. From Eq. (2.4), the electron temperature is calculated from the function of I through $v_e = \sqrt{T_e/m_e}$, and a sound speed is a function of an electron temperature by

$$C_s = \sqrt{\frac{(1+Z)T_e}{Am_p}} \tag{2.5}$$

In a classical ablation model [14], ablated mass is assumed to blow off at critical density point at the sound speed. Therefore, the mass ablation rate can be described as $\dot{m} = \rho_c C_s$ where ρ_c is a mass density at a critical density point and ablation pressure is described as $P = 2\dot{m}C_s$, which can be calculated by [10]

$$P = 2\dot{m}C_s \sim 0.9\frac{1+Z}{Z}\left(\frac{I_{14}\lambda_{\mu m}^2}{f}\right)^{\frac{2}{3}}\frac{1}{\lambda_{\mu m}^2}\ [\mathrm{TPa}] \tag{2.6}$$

Fig. 2.4 shows the scaling of ablation pressure as a function of an absorbed laser intensity by using Eq. (2.6) with $Z = 3.5$ and $\lambda_{\mu m} = 0.351$ [10]. High intensity laser around 10^{15} W/cm^2 is required to create ~10 TPa pressure for ICF. It should be noted that collisional absorption decreases with increasing laser intensity. Therefore, an absorbed laser intensity deviates from the irradiation laser intensity in a high-intensity regime (more than ~10^{15} W/cm^2), which indicates that ablation pressure shows saturation tendency as a function of irradiation laser intensity.

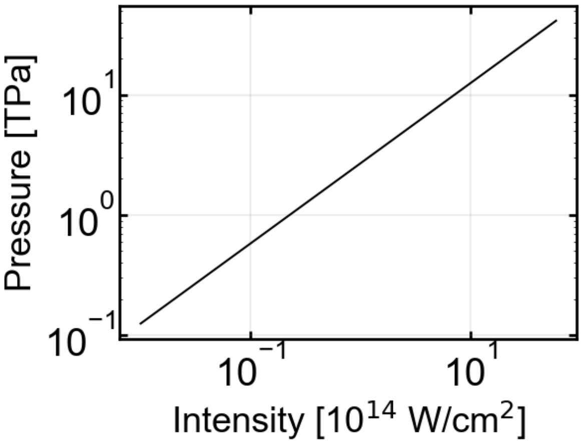

Figure 2.4. Ablation pressure as a function of laser intensity.

An order estimation of required laser energy is also shown by considering the internal energy of solid DT fuel. Here, for the simplest discussion, energy for hot spot formation was ignored because it consists of a relatively small portion. The internal energy of DT fuel per unit mass can be estimated by [10]

$$E_c = \frac{3\varepsilon_f/5}{m_{DT}}\alpha_F \tag{2.7}$$

Here, $\varepsilon_f = (1/8)(3/\pi)^{2/3}h^2{n_e}^{2/3}/m_e$ is a fermi energy of an electron, and α_F is an isentropic parameter to measure deviation from the fermi degeneracy, which should be as small as possible. When solid DT is compressed 1000 times, and α_F is assumed to be 3, E_c is calculated to be 33 MJ/g. When the total mass of DT ice is ~ 3 mg, an internal energy is calculated to be $33\ \mathrm{MJ/g} \times 3\ \mathrm{mg} \sim 100$ kJ. When assuming a conversion efficiency of internal energy from a laser as around 10 % [10], these estimations indicate that MJ class laser is required in ICF. For example, Canaud *et al.* calculated a target gain of 60 with a

1.5 MJ laser [15].

These high-intensity and high-power laser demands motivated the construction of giant laser facilities worldwide [16–21]. The most powerful laser in the world can produce 2.2 MJ by 192 beams at the National Ignition Facility (NIF) at Lawrence Livermore National Laboratory (LLNL) as of September 2023 [20]. The most powerful laser in Japan is the GEKKO-XII laser at Osaka University, where the laser experiments in this dissertation were performed and can produce ~8 kJ by 12 beams [21]. The laser energy at GEKKO-XII is not enough for ignition experiments. However, laser intensity can be up to 10^{16} W/cm^2 by focusing a laser on a target plane, which is high enough to explore physics related to ICF. Those facilities employ laser energy amplification in glass excitation. Amplification was performed through a long pass by extending its spatial width to avoid damaging optics. Fig. 2.5 shows amplification passes of GEKKO laser beams as one example.

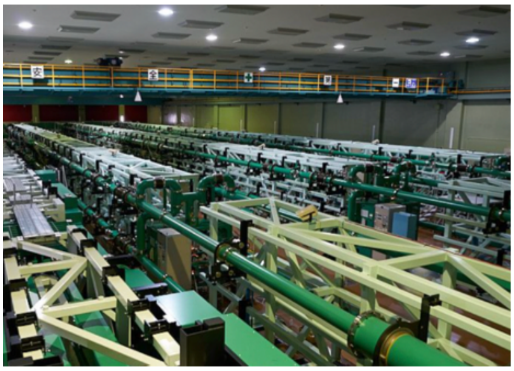

Figure 2.5. Laser amplifier of GEKKO-XII.

2.5. Issues

We can achieve a high gain ignition by imploding a small low Z capsule that contains two-layered DT fuels by a high-intensity and high-power laser from the above section, which is not as straightforward as it sounds due to some detrimental issues. Ablation surface perturbations due to non-uniform laser irradiation and incompleteness of capsule fabrication are critical issues to prevent ignition because such perturbations are amplified during implosion by RT instability, destroying a shell or/and decreasing the temperature and volume of a hot spot [22–24]. RT instability is seen at the interface of two fluids with different densities in an acceleration field pointing toward the lighter fluid. In RT instability, the growth of sinusoidal modulations (wavenumber k) with the acceleration g at the interface between a low-density ρ_1 and a high-density ρ_2 fluids is described by [1]

$$\zeta = \zeta_0 exp(\gamma_{cl} t) \tag{2.8}$$

Where $\gamma_{cl} = \sqrt{Agk}$, $A = (\rho_2 - \rho_1)/(\rho_2 + \rho_1)$, and ζ_0 is an initial amplitude. In ablative plasma, it is known that the RT growth is suppressed more than classical growth, thanks to ablative stabilization [25,26].

$$\gamma = \sqrt{\frac{kg}{1 + kL}} - \beta k v_a \tag{2.9}$$

Here, L, v_a, and β are a plasma density scale length, an ablation velocity, and a dimensionless value, respectively. Since growth rate is a function of modulation wavelength, RT instability is analyzed based on a mode number $l = 2\pi R/\lambda$ where R is a capsule radius. In the acceleration phase, the interface between a low-density plasma and a dense shell is unstable, and therefore, outer surface perturbations grow according to Eq. (2.9). The most unstable mode in this stage is usually $l = 100{\sim}300$, with a corresponding growth rate of ~1000 [27]. When perturbations become comparable with the shell thickness, it leads to the destruction of a fuel shell. Here, it should be noted that the perturbations also grow in the inner surface of the shell with the amplitude reduced by a factor of $\exp{(-l\delta R/R)}$. Such a phenomenon of the transmissions of a perturbation is called feed-through [28,29], and the inner surface perturbations become unstable in the deceleration at the interface of a low-density hot spot and a high-density cold shell, resulting in the decrease of hot spot volume and temperature. For the simple estimation of the degradation due to the decrease in hot spot volume, the number of neutrons from fusion reactions is estimated. The number of neutrons generated inside the hot spot is described by $N = n_D n_T \langle \sigma v \rangle V_{hot} \sim (4/3)\pi R_{hot}^3$. When there is a perturbation ζ_{in} on the inner surface, the effective radius of the hot spot is regarded as $R_{eff} = R_{hot} - \zeta_{in}$. Therefore, the number of neutrons generated inside the hot spot decreases with $(R_{hot} - \zeta_{in})^3$. When the perturbation reaches the half of a hot spot radius, the generated neutrons decrease to ~ 10% [27].

2.6. Approaches to address issues

Various works have been done to address the issues described above. To obtain better irradiation uniformity, phase plates such as random phase plate (RPP) [30] and kinoform phase plate (KPP) [31] were developed, and further improvement to incorporate temporal smoothing techniques such as induced spatial incoherence (ISI) [32] and smoothing by spectral dispersion (SSD) [33] were also developed. Those techniques are employed in high-power laser facilities. Another notable approach to mitigate drive beam non-uniformity is indirect-drive ICF [34]. The basic concept of this approach is shown in Fig. 2.6 (a). A fuel capsule is placed inside a hohlraum of high Z element, and lasers irradiate the inside of the hohlraum. As a result, laser-converted X-rays with high uniformity implode a fuel capsule. After tremendous efforts to minimize initial ablation surface modulations and their growth by hydrodynamic instabilities, scientists achieved ignition using indirect-drive ICF at LLNL in December 2022 [5–7], which is regarded as the most significant breakthrough in ICF research history. On the other hand, indirect-drive ICF is not the best in the IFE application because of its low conversion rate of X-rays from laser and the complex target design, which is difficult to apply to repetition laser irradiation required in ICF power plant [35]. For the IFE application, the direct-drive approach is advantageous because of its simplicity and higher efficiency. To mitigate laser imprinting, a target-based approach was investigated; a foam ablator [36], a high Z dopant ablator [37], and a diamond ablator [38] were suggested, which is explained in the next chapter in more detail. Moreover, advanced ICF schemes such as fast ignition (FI) scheme [39] and shock ignition (SI) scheme [40] were proposed. For FI and SI schemes, implosion and ignition are separated to avoid rapid implosion to mitigate RT instability growth. In FI scheme, DT fuel is ignited by relativistic electrons (~MeV) produced with an ultra-intense short laser irradiation of 10^{18} ~10^{20} W/cm^2. In FI scheme, to prevent plasma from filling the pass of the ultra-intense laser, a cone target is typically employed as shown in Fig. 2.6 (b) [41,42].

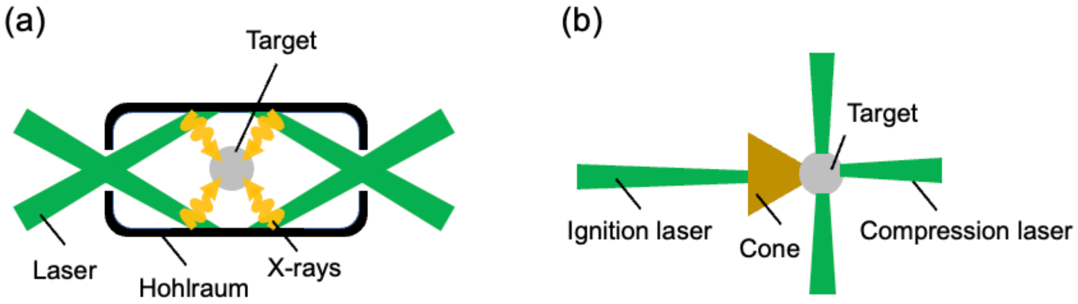

Figure 2.6. Basic concept for (a) indirect-drive ICF and (b) fast ignition (FI) scheme. In FI, the compression and ignition pulses are drawn in the same picture, whereas the ignition pulse is launched after the compression pulse.

2.7. Shock ignition (SI) scheme

SI scheme is a relatively new scheme that was proposed by Betti et al. in 2007 [40]. In SI scheme, a low-intensity laser pulse of ~10^{14} W/cm^2 compresses a target, and DT fuels are ignited by a converging shock wave produced by a higher-intensity spike pulse of several 10^{15} to 10^{16} W/cm^2. A schematic example of a laser pulse is shown in Fig. 2.7. Slow implosion in the compression phase can avoid the growth of RT instability. In addition, a larger fuel mass can be imploded compared with a conventional implosion in the same laser energy, resulting in higher efficiency. Moreover, this scheme does not require a complicated target in indirect drive ICF, nor an additional ultra-intense laser required in FI scheme.

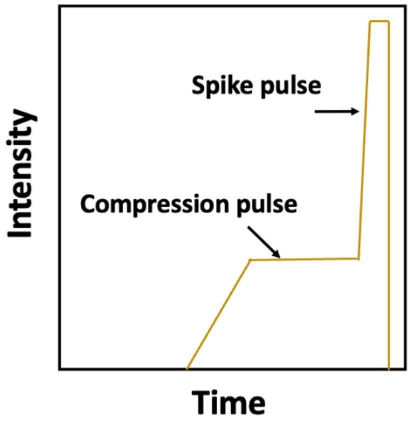

Figure 2.7. Example of the laser pulse in SI scheme.

The most significant milestone for SI scheme is the creation of shock pressure enough to ignite a hot spot; typically, an ablation pressure of 30 TPa is required [43]. This is why spike pulse intensity is envisaged to have more than several 10^{15} W/cm^2. However, in such a high-intensity regime, the laser absorption by collisional absorption decreases, and laser-plasma interactions (LPIs) such as stimulated Raman scattering (SRS) and two plasmon decay (TPD) become dominant, leading to hot electron (HE) generation. In ICF, HE generation is generally considered detrimental because it preheats fuels before compression [44,45]. Therefore, HEs should be suppressed in the implosion phase. On the other hand, a high-intensity spike pulse in the SI scheme is launched in the ignition phase when the areal density of the shell already increases by a factor of 10 to 20 and therefore HEs of not too high energy (typically less than ~100 keV) are expected to be absorbed in the outer region of the shell [40]. As a result, HE does not preheat fuels; instead, it is expected to enhance ablation pressure [46–49]. From the above, HEs could be a critical factor in SI scheme, and understanding LPIs and HE generation is of great importance.

2.8. Role of this dissertation

Diamond target is a low Z element material, it can mitigate laser imprinting, it can be used together with other techniques such as high Z coating, and it can be applied to advanced schemes in direct-drive ICF such as SI scheme. These advantages of the diamond target make it attractive as a fuel capsule for direct-drive ICF in the future. This dissertation focused on diamond targets and tried to establish fundamental technologies to fabricate diamond capsules. Also, this study tried to improve the understanding of LPIs and HE generation in diamond targets to apply them to direct-drive ICF.

In Chapter 3, the fabrication of diamond capsules in a way that can apply to mass production was investigated, and the fabricated diamond capsules were comprehensively characterized. Also, laser irradiation experiments were performed to demonstrate its quality and characterization accuracy. The results indicated that the established fabrication process in this study is promising to supply them in the future power plant.

In Chapter 4, LPIs and HEs were experientially explored in diamond targets. In this study, an experimental platform that enables the characterization of LPIs and HEs was developed, and those were characterized in plastic targets, which is the most typical ablator material, and then, LPIs and HEs in diamond target were explored in comparison with plastic targets. The results revealed the effects of hydrogen (H) in the ablator material, and the design of diamond targets in terms of LPIs and HEs for direct-drive ICF application was suggested.

3. Development of diamond capsules

3.1. Diamond ablator for direct-drive ICF

Diamond target can mitigate laser imprinting thanks to its low compressibility and higher density than conventional ablator materials. Here, the modeling of laser imprinting explains the importance of material compressibility and density [27,38]. Fig. 3.1 shows the schematic of the formation of laser imprinting by non-uniform laser irradiation.

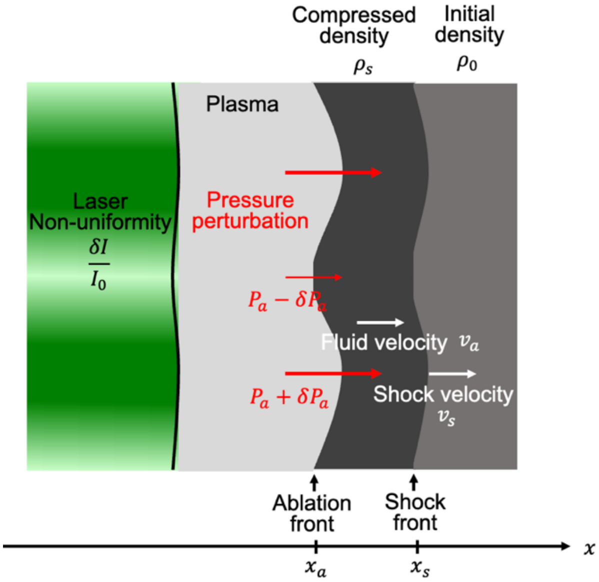

Figure 3.1. Illustration of laser imprinting due to non-uniform laser irradiation.

Irradiation with non-uniformity with $\delta I/I_0$ produces the pressure perturbation δP_a, which introduces non-uniform fluid velocity δv_a with rippled shock propagation. From the equation of motion, the time derivative of the momentum perturbations per unit surface should be equal to the pressure perturbation on the ablation front [27] when flow in the lateral direction can be neglected, obtaining

$$\frac{\partial\delta\left(MV_{depth}\right)}{\partial t} = \delta P_a \tag{3.1}$$

Considering the momentum perturbation and velocity perturbation on the shock front in an incompressible fluid model, Eq. (3.1) can be simplified into

$$2\delta v_a \rho_s (v_{s0} - v_{a0}) = \delta P_a \tag{3.2}$$

Here subscript 0 denotes unperturbed quantities. The imprint amplitude δx_a is obtained from Eq. (3.2)

$$\delta x_a = \int_0^t \delta v_a dt$$

$$\delta x_a = \int_0^t \frac{\delta(P_a)}{2\rho_{s0}(v_{s0} - v_{a0})} dt \tag{3.3}$$

As shown in the previous section, laser energy is absorbed in a low-density plasma by collisional absorption, and the absorbed energy is then transported to the ablation surface by electron thermal conduction. Here, pressure perturbations are relaxed by diffusive electron's thermal conduction, which is called thermal smoothing effect, and it is given by cloudy-day model [50] by

$$\delta P_a = \frac{2}{3} P_0 \frac{\delta I}{I_0} exp(-kD_{sb}) \tag{3.4}$$

Here, D_{sb} is the effective separation from a point where the laser is absorbed to the ablation front (so-called standoff distance). The exponential term indicates that the thermal smoothing effect becomes effective when the standoff distance is large. Many works tried extending a standoff distance using techniques such as a foam target [36,37] and high Z coating. However, in early irradiation timing and when wavelengths of modulations are long, the thermal smoothing is not effective. Based on the conservation of mass across a shock wave, the relation Eq. (3.5) can be obtained [13].

$$\frac{\rho_s}{\rho_0} = \frac{v_{s0}}{v_{s0} - v_{a0}} \tag{3.5}$$

This means that material of low compressibility can reduce laser imprinting through $(v_{s0} - v_{a0})$. Also, the term of ρ_{s0} in Eq. (3.3) indicates that high material density reduces an imprint amplitude. Diamond is a stiff material with the lowest compressibility under dynamic compression [51], and it has a higher density (~3.5 g/cm^3) than conventional capsule materials such as plastic (~1 g/cm^3). The reduction of laser imprinting, thanks to material stiffness and density, is effective even in early irradiation timing and when modulation wavelengths are long, making diamond an attractive material for direct-drive ICF targets.

3.2. Significance of this study

Diamond capsules were first developed by J. Biener *et al.* in 2009 for the application to indirect-drive ICF [52]. Here, it should be noted that diamond is also attractive in direct-drive ICF owing to its higher density than conventional ablator materials (i.e., plastic, etc.) [53,54]. In the fabrication work, microwave plasma chemical vapor deposition (MP-

CVD) technique was employed for the diamond deposition, and the capsule surface was polished to obtain high surface uniformity [52]. Also, Ding *et al.* demonstrated the fabrication of diamond capsules by the high-pressure and high-temperature (HPHT) method for the direct formation of diamond from amorphous carbon deposited by MP-CVD [55]. On the other hand, the deposition area of MP-CVD is limited by microwave wavelength, and therefore, it is not necessarily suitable in terms of mass production. Also, the voids and pits are seen in diamond capsules, which requires further improvement of capsule quality, although the improved capsule quality of diamond capsules in recent years already contributed to the breakthrough at LLNL in 2022 [5–7]. Kato *et al.* developed a basic fabrication process for diamond capsules by employing hot filament chemical vapor deposition (HF-CVD) technique [56]. In HF-CVD, the deposition area can be easily extended only by increasing the number of filaments, and therefore, it is ideal for mass production [57]. However, there were technical issues that should be addressed in the fabrication process. Also, the fabricated diamond capsules were not characterized in detail. In this study, the improvement of the fabrication process is shown, and the fabricated diamond capsules were comprehensively characterized. Moreover, the implosion experiments were performed to demonstrate fundamental capsule quality and the characterization accuracy. These results indicate that the fabrication process established in this study is promising to apply them into the future power plants.

3.3. Fabrication of diamond capsules

3.3.1. Diamond deposition

In HF-CVD, hydrogen (H) and carbon (C) sources are dissociated into radicals by heating hot filaments. H radicals selectively etch the sp^2 bond (graphitic component); therefore, the growth of the sp^3 component (diamond) predominates. Fig. 3.2 shows the experimental setup for diamond deposition using HF-CVD technique.

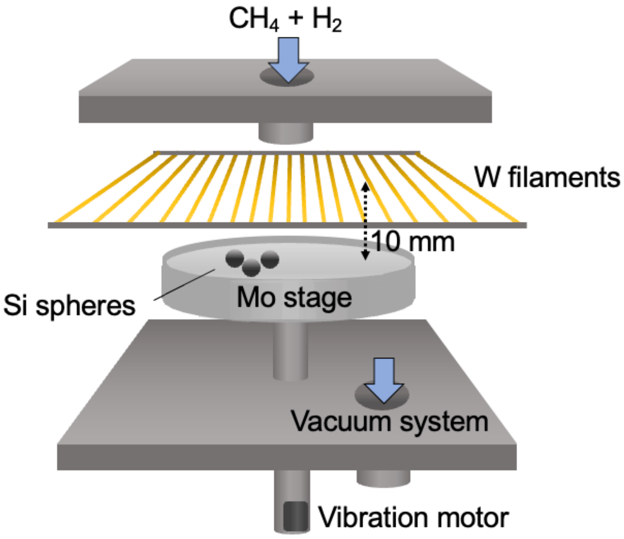

Figure 3.2. Experimental setup for diamond coating on Si sphere by HF-CVD technique.

As hot filaments, an array of 19 parallel tungsten (W) wires ($\phi = 0.12$ mm) was resistively heated to ~2300 °C. Deposition duration was set to 1 to 4 hours. As a substrate, a Si sphere of a typical diameter: 0.48 mm was set on the molybdenum (Mo) stage, where the distance from the filaments was 10 mm. Note that the Si sphere had been subjected to typical preprocessing (i.e., scratching by a diamond powder slurry) to enhance the nucleation density in advance. Gas pressure in the chamber was set to 10 torr with hydrogen (H_2) at 1000 standard cubic centimeter per minute (sccm). Here, methane (CH_4) flow was chosen as a variable, ranging from 10 to 30 sccm (1% to 3%), and the tendency of decreasing grain size of polycrystalline diamond with increasing CH_4 concentration was obtained as shown in Fig. 3.3.

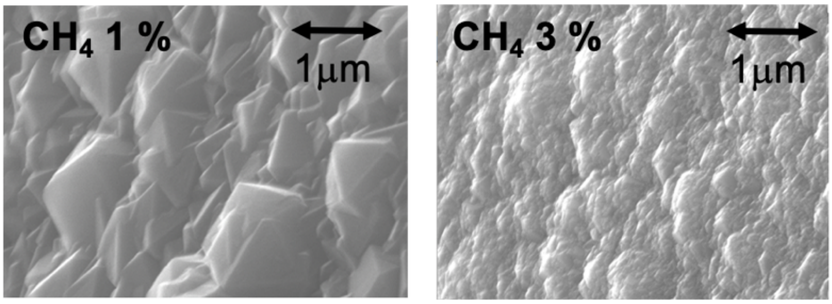

Figure 3.3. Surface morphology in SEM images for different CH_4 concentrations.

Such tendency is explained by the high nucleation rate due to higher CH_4 concentration. To realize high surface smoothness, a 3% CH_4 concentration was employed for typical conditions in this dissertation because diamond with small grain sizes was expected to have smaller surface roughness. During deposition, the Si sphere was rotated by the vibration of the Mo stage to deposit diamond all over the sphere. The vibration rate was initially set to 30 seconds every 15 minutes. However, some of the diamond spheres were found to be stuck onto the Mo holder during deposition, significantly impairing the capsule quality. This problem was because the diamond was deposited not only on the Si spheres but also on the Mo stage. This issue was easily solved by employing a higher vibration rate: 30 seconds every 5 minutes. The improvement of diamond quality thanks to a high vibration rate is shown in Fig. 3.4. It should be noted that an even higher vibration rate would be ideal. However, to avoid any problems related to chamber leaks due to vibration, the vibration rate of 30 seconds every 5 minutes was employed as a typical condition in this study.

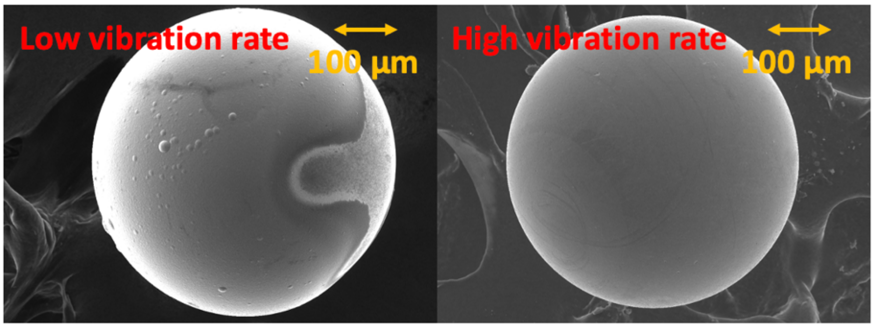

Figure 3.4. Whole view of diamond spheres in SEM for different vibration rates.

3.3.2. Etching Process

The fabricated diamond-coated Si spheres were cleaned using a mixed acid (96 wt% H_2SO_4:61 wt% HNO_3 = 3:1) at ~250 °C to remove any graphitic contents and debris on the surface of the diamond spheres. Then, cleaned spheres were subjected to the etching process of the Si mold. In the first step, the diamond sphere was drilled using a femtosecond laser to make a 10 µm diameter hole, and the Si mold inside the capsule was removed through the hole by soaking diamond spheres in hydrofluoric acid/nitric acid mixture (50 wt% HF:61 wt% HNO_3 = 3:1) solution. However, the preliminary laser irradiation experiment revealed the existence of Si residual inside a diamond sphere. Fig. 3.5 (a) and (b) show the implosion trajectory from an X-ray streak camera and the image from an X-ray pinhole camera.

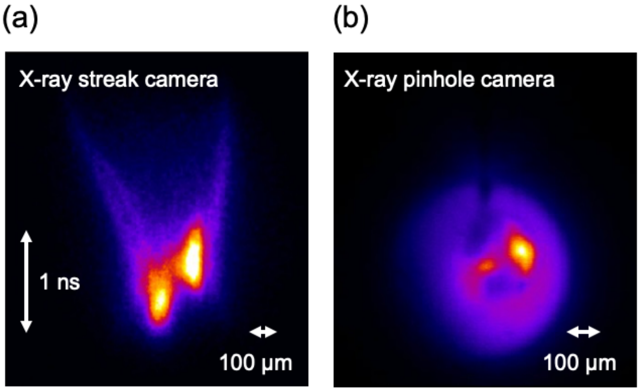

Figure 3.5. Implosion image of diamond capsules for an X-ray streak camera and an X-ray pinhole camera in preliminary laser irradiation experiment.

Significant asymmetry and abnormal X-ray emissions were observed, which were attributed to mass non-uniformity and line X-rays due to Si residuals inside the diamond capsule.

The Si residuals in the etching process were mainly attributed to two factors. The first factor is that the diamond capsule rise onto the solution surface when buoyancy inside the capsule become significant, which stops reactions from proceeding. The second factor is due to the large surface tension at the hole of 10 μm. The reaction proceeds by reaction gases going out as bubbles. The surface tension exserted at radius R of fluid is estimated from the Laplace-Young equation: $P = 2\gamma/R$ where γ is the fluid's viscosity. When R is regarded as a small value, an order of hole size (i.e., 10^{-5} m), surface tension becomes large, which is not negligible. It is supposed that in early times, reactions are active, and therefore, the gas pressure inside a capsule overcomes surface tension at the interface of the acid solution, and a reacting gas can go out. Once a reacting gas goes out of a capsule, the pressure inside the sphere becomes low; therefore, the fresh acid solution gets into the inside. Such repetition continues until the reacting gas pressure becomes low and stops its cycle. To solve the first problem, the diamond sphere was stuck on the bottom of beaker by clay, and the clay was removed after the etching of the Si mold with acetone. To solve the second problem, an external pressure was introduced by using ultrasonic vibration. The schematic image of the improved etching process is shown in Fig. 3.6.

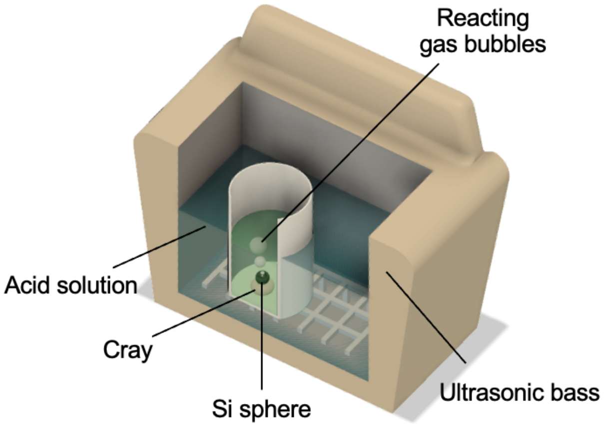

Figure 3.6. Si etching by acid solution with ultrasonic vibration.

3.4. Characterization of diamond capsules

The fabricated diamond capsules were comprehensively characterized. Not only the typical parameters of diamond films (i.e., surface morphology and sp^2 content) but also parameters important for direct-drive ICF applications (W and H contents, capsule thickness, density, and mode amplitudes of surface roughness) were characterized in detail.

3.4.1. Surface Morphology and Sp^2 Content

The surface morphology was evaluated using scanning electron microscopy (SEM) and atomic force microscopy (AFM). Fig. 3.7 shows a typical microscopic view from SEM and an altitude image from AFM.

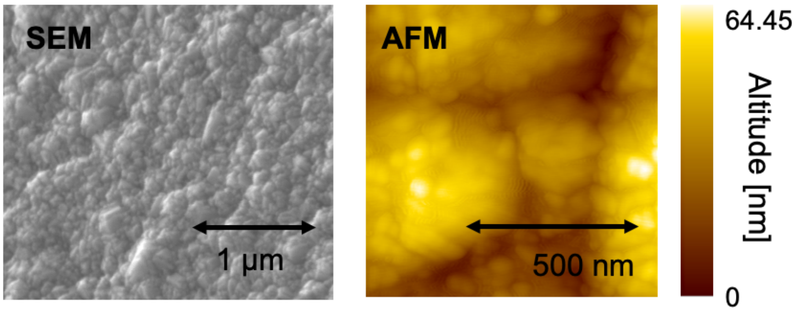

Figure 3.7. Microscopic view of diamond surface from SEM and AFM.

In both images, nanocrystalline grains of round shapes were observed, and the root mean square (RMS) value was evaluated to be 11 nm from the AFM data in Fig. 3.7, showing small surface smoothness. On the other hand, the dome-shaped hills of several micrometers in diameter were also observed in macroscopic SEM observation, as shown in Fig. 3.8. This could be attributed to the incorporation of debris during the deposition process that should be suppressed in future work.

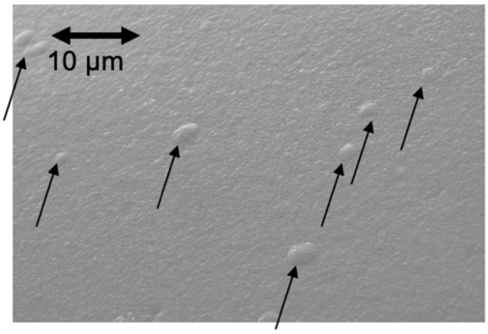

Figure 3.8. Macroscopic view of diamond surface in SEM image.

Sp^2 content was discussed using Raman spectroscopy with $\lambda = 532$ nm laser excitation. Fig. 3.9 shows the Raman spectrum after subtracting background linearly.

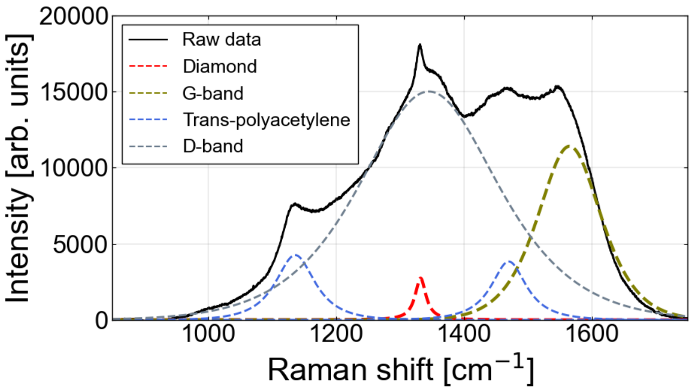

Figure 3.9. Raman spectrum with multi-Voigt function fitting.

Multiple peaks were observed, including diamond, G-band, trans-polyacetylene (C_2H_2), and D-band peaks, as shown in multi-Voigt function fitting. These multiple peaks are typically observed in nanocrystalline diamond. D band and G band indicate sp^2 contents [58–63]. Note that the Raman cross-section of these peaks is much larger than the diamond peak by a factor of typically 50–230 [64,65]. The trans-polyacetylene peak indicates that the diamond film contains H [66,67], which is quantitatively evaluated by SIMS evaluation in the next section.

3.4.2. W and H Contents

Hydrogen (H) and tungsten (W) are typical non-diamond contents in diamond deposited in HF-CVD technique, and those are attributed to hydrocarbon source gases and hot filaments, respectively. In direct-drive ICF, H and W are known to change LPIs and radiation. High H concentration enhances LPIs and HE generation, which is discussed in the next chapter. W enhances radiation, causing fuel preheating. The W and H contents were measured using secondary ion mass spectroscopy (SIMS), which was absolutely calibrated by a standard diamond sample of known H and W concentration. Here, SIMS was performed on a diamond film deposited on the Si plate (thickness: 0.53 mm) in the same deposition conditions as the spheres. Fig. 3.10 shows the results of SIMS for H and W concentration profiles.

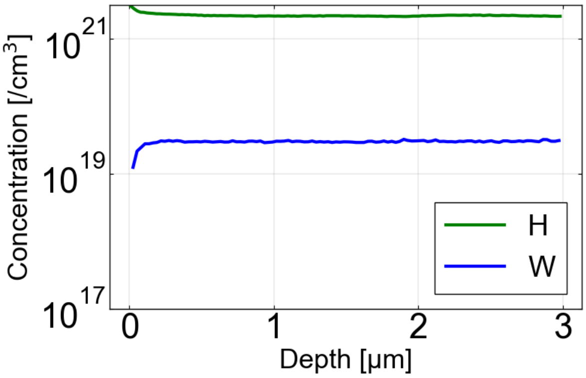

Figure 3.10. Depth profile of H and W concentration from SIMS. This corresponds to 1.2 at. % of H concentration and 0.017 at. % of W concentration.

The concentration of H was 2.2×10^{21} /cm^2, corresponding to 1.2 at. % compared to the number density of single-crystal diamond (1.8×10^{23}/cm^2). For W, the concentration was 3.0×10^{19} /cm^2, corresponding to 0.017 at. %. 1.2 at. % of H concentration might slightly enhance HE, as discussed in detail later. W incorporation is very low and seems negligible, but quantitative evaluation should be done carefully in the future.

3.4.3. Thickness and Density

Thickness and density are crucial parameters because they directly determine the implosion dynamics. To evaluate the thickness, a two-step procedure was employed in which the radius difference of a spherical sample before and after diamond deposition was evaluated. An optical microscope [68] was developed to evaluate the radius precisely. Fig. 3.11 shows the entire view of the developed microscope system.

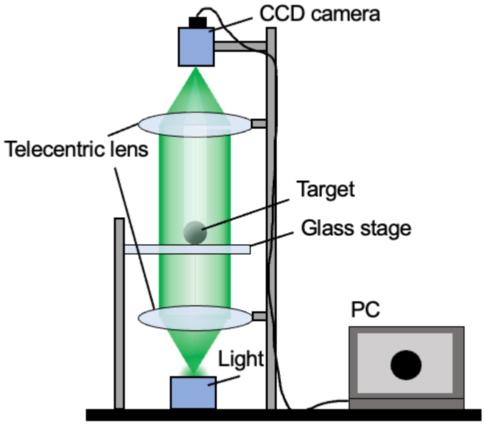

Figure 3.11. Schematic of a developed optical microscope.

In the system, a telecentric lens was employed for the focusing lens. A telecentric lens enables the observation of an object with a small magnification deviation because it only images parallel light. The obtained image was introduced to image data analysis, the flow of which is summarized in Fig. 3.12.

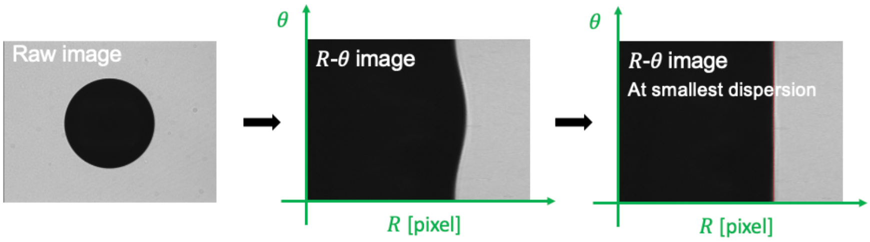

Figure 3.12. Flow of image data analysis.

A polar transformation ($x - y$ plane to $r - \theta$ plane) was performed based on the assumed center, and border points (radius) were determined with sub-pixel accuracy by fitting the sigmoid function to calculate the dispersion of radius over θ. By reiterating this process for different centers, the center was determined to have the smallest dispersion. Thus, the radius can be calculated by averaging the radius values over θ. In addition, the data of the smallest dispersion are utilized for the evaluation of the mode analysis in the later section. For the absolute calibration of the developed microscope system, steel spheres of known diameters were evaluated, and it was verified that the spatial scale of the system was 0.7260 µm/pixel. The accuracy of the average radius evaluation was 0.1 µm, which led to a thickness evaluation of 0.1 µm accuracy. Fig. 3.13 shows the results of the thickness evaluation of several nanocrystalline diamond samples with different deposition times, where the size of the marker represent the error bar.

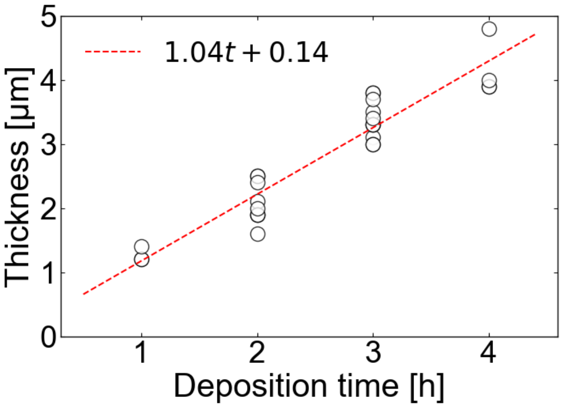

Figure 3.13. Thickness of diamond capsules at different deposition times.

It was shown that the thickness can be controlled by deposition time as shown in the thickness function, h [μm] = 1.04 t [h] + 0.14. Note that the offset of 0.14 μm came from the diamond deposition in the filament conditioning period prior to the deposition process.

The density of the nanocrystalline diamond was also evaluated using a two-step procedure for the mass difference of the sphere before and after diamond deposition, and the mass difference was divided by the capsule volume. For mass measurements, an ultra-micro balance (METTLER TOLEDO, UMX2) with a minimum scale of 0.1 μg was employed. The capsule volume was calculated from the thickness data obtained using the developed optical microscope. As a result, the density was evaluated to be 3.2±0.2 g/cm^3. The lower density value than single crystal diamond (3.5 g/cm^3) can be reasonably explained by incorporating sp^2 contents as described in section 3.4.1.

3.4.4. Mode Amplitudes of Surface Roughness

The surface roughness of a fuel capsule is a critical factor in ICF because even a small non-uniformity is amplified by RT instability during implosion. In ICF applications, the surface roughness is typically evaluated based on the mode number *M*, which is defined by *2πR/λ*, where *R* is a capsule radius and *λ* is a modulation wavelength. Typically, it is pointed out that only nanometer-amplitude modes are acceptable for the realization of ignition [69]. Mode analysis was performed using a Fourier transformation of the surface roughness data. To evaluate low modes (large-scale modulations), a telecentric image was analyzed, and the amplitudes of modes less than 150 were evaluated. There were no mode amplitudes larger than 0.1 μm, which is the resolution limit of the telecentric imaging system. It should be noted that mode 1 non-uniformity (i.e., non-concentricity of the coating) cannot be evaluated in this method. Evaluation of mode 1 should be performed in future work. For the evaluation of high modes (small-scale modulations), AFM data of 10 μm × 10 μm were analyzed, and the amplitudes of modes greater than 150 were evaluated, as shown in Fig. 3.14. Typical values of the high modes are less than 40 nm, which is reasonably comparable to the RMS values of the surface roughness mentioned in section 3.4.1. It should be noted that the Si spheres before the diamond deposition also had comparable surface roughness, which should correspond to the inner surface roughness.

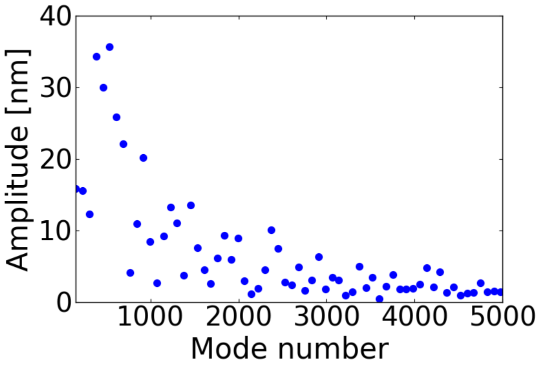

Figure 3.14. Amplitudes of high modes evaluated by mode analysis in AFM data.

3.5. Laser irradiation experiment

3.5.1. Experimental conditions

Characterized hollow diamond capsules were introduced into direct-drive laser irradiation experiments at the GEKKO-XII laser facility at Osaka University. Experiments were performed at target chamber I, where a target can be spherically irradiated by 12 high-power laser beams, as shown in Fig. 3.15.

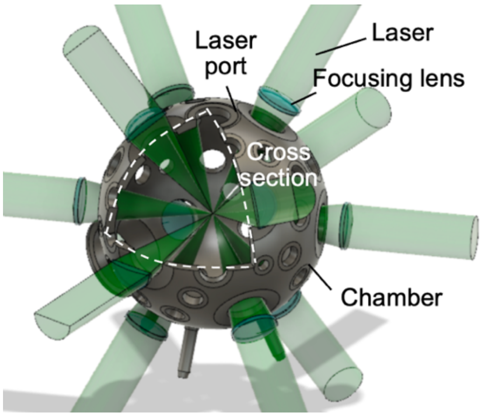

Figure 3.15. Image of target chamber of GEKKO-XII with laser irradiation.

12 amplified beams were introduced to the center of the target chamber of $\phi \sim 1.7$ m by focusing a lens with a *F-number* of 3 through laser beam ports. The focusing lens position was set to $d/R = -5$, where d is the lens position from the best focus position, R is the radius of the capsule, and the negative sign indicates that the lens is closer to the target from the position of best focus. The pulse shape was Gaussian, with a duration of 1.3 ns. The total energy of the laser light was typically 3 kJ.

3.5.2. Plasma Diagnostics

To comprehensively evaluate capsule implosion, three types of X-ray diagnostics were employed. Fig. 3.16 shows the plan view of the target chamber at the location of each diagnostic where the direction cosine *(x,y,z)* is shown in italic letters. X-ray emissions are supposed to be the strongest at the ablation front, as defined by the maximum value of $n_e^2\sqrt{T_e}$, where n_e and T_e are the electron density and electron temperature, respectively, when assuming thermal bremsstrahlung. Therefore, the implosion trajectory of a capsule can be evaluated by following the maximum X-ray emissions. Two X-ray streak cameras (XSC1 and XSC2) were used to evaluate the one-dimensional time-resolved implosion trajectory. The magnification and sweep time window were 10.3 and 4.81 ns for XSC1, respectively, and 9.5 and 5.62 ns for XSC2, respectively. Considering the pinhole diameter and cathode width of each XSC, the spatial and time resolutions were calculated to be 27 μm and 90 ps for XSC1, respectively, and 28 μm and 89 ps for XSC2, respectively. An X-ray framing camera (XFC) was employed in order to evaluate two-dimensional implosion performance at six consecutive timings (+0ns, +0.1 ns, +0.2 ns, +0.23 ns, +0.33 ns, and +0.43 ns). The magnification was 14.4, and the spatial resolution was 27 μm. Two X-ray pinhole cameras (XPHC1 and XPHC2) were employed to evaluate the time-integrated information on the overall implosion. The magnification and spatial resolution were 8.8 and 28 μm for XPHC1, respectively, and 4.4 and 31 μm for XPHC2, respectively. Note that the x-ray energy range of all diagnostics was observed to be more than 1 keV owing to a Be filter of 50 μm, which enabled the exclusion of contributions from line X-rays of carbon.

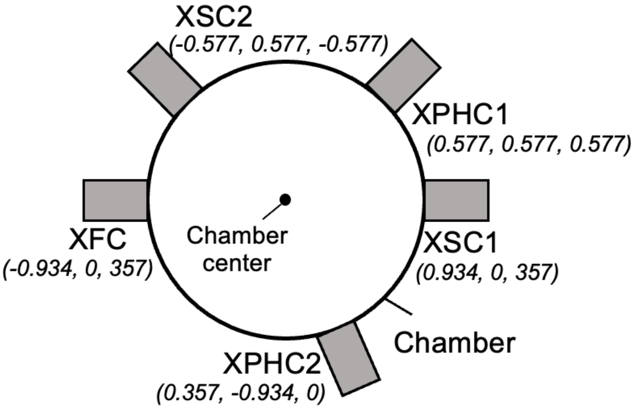

Figure 3.16. Configuration of X-ray diagnostics. Direction cosine (x,y,z) of each diagnostic is shown in italic letters.

3.5.3. Experimental results

As targets, three nanocrystalline diamond capsules (thickness: 2.6 µm, 3.1 µm, and 4.0 µm) were introduced into the experiment. Those capsules were glued with ultraviolet-curing resin onto a glass stalk and introduced into the chamber center. An optical image of the nanocrystalline diamond target is shown in Fig. 3.17.

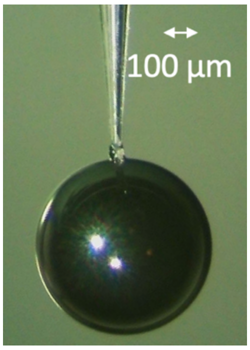

Figure 3.17. Optical image of a hollow nanocrystalline diamond target for laser irradiation experiments.

Those capsules were successfully imploded, different from preliminary implosion experiments. Herein, the experimental results of a 3.1 μm-thick hollow nanocrystalline diamond capsule are shown, where the complete dataset of all the diagnostics is obtained without any failures. In the 2.6 μm-thick diamond capsule shots, two laser beams were lacking due to technical issues, and in the 4.0 μm-thick diamond capsule shot, one of the X-ray diagnostics was lacking due to technical issues.

Fig. 3.18 shows the results for XSC1. We can see the implosion trajectory in the form of X-ray emissions from the ablation front. The time axis was shown, assuming a peak laser timing of 0 ns. The left and right trajectories are symmetrical, and x-ray emissions reach their maximum value at peak compression timing, which means that kinetic energy is converted to thermal energy owing to collision at the center of the capsule. This verifies that the capsule is successfully compressed, unlike in a preliminary experiment where significant implosion non-uniformity and abnormal X-ray emissions were observed. Notably, XSC2 also showed successful implosion, which is not shown here. As an analysis, the implosion trajectories (i.e., plots of the capsule radius as a function of time) were evaluated from the peak X-ray emission points over time. The results are compared with the one-dimensional radiation hydrodynamic simulation in the next section.

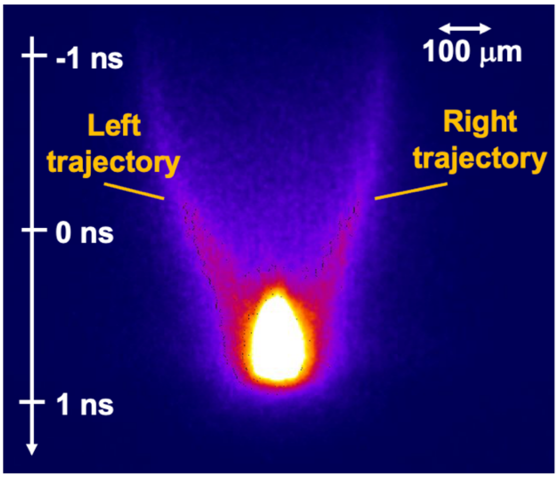

Figure 3.18. One-dimensional implosion image from a streaked image of the XSC1.

Fig. 3.19 shows the XFC image. The XFC captures the early midpoint of the implosion, 0–0.43 ns. The white dotted circle indicates the initial size of the capsule. A two-dimensional compression trajectory is observed through X-ray emissions from the ablation front, showing a successful capsule implosion two-dimensionally without implosion failures due to capsule incompleteness, at least in current resolution. In the images, X-ray emissions from the resin and stalk were also observed, and the X-ray emissions from the capsule center before peak compression are explained by the prior collision of light blowoff plasma from the inner surface of the capsule.

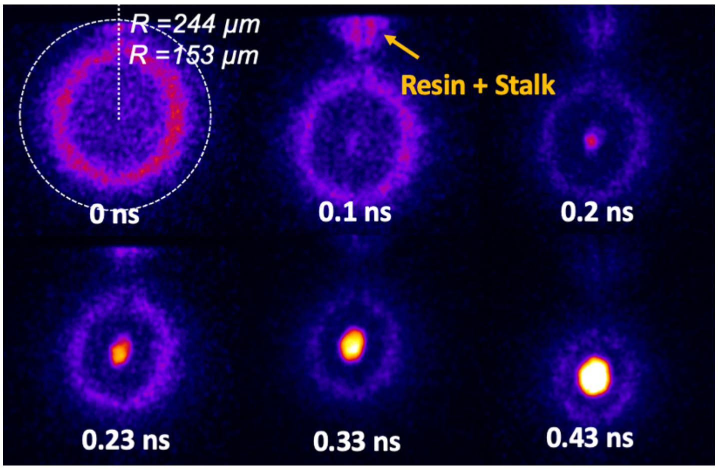

Figure 3.19. Two-dimensional implosion image in 6 different times from the XFC image.

Mode analysis was performed by polar transformation of the XFC image to determine implosion non-uniformity, as shown in Fig. 3.20 (a), where the green line indicates the plots of peak X-ray emission points. Note that non-uniformity at 0.43 ns cannot be obtained since strong X-ray emissions from the center obscure the ablation front emissions. Fig. 3.20 (b) shows the mode amplitudes at 0.33 ns as one example. Mode amplitudes of less than 8 are shown because there are no large amplitudes in more than mode 8 in our analysis. Implosion non-uniformity was observed in mode 2.

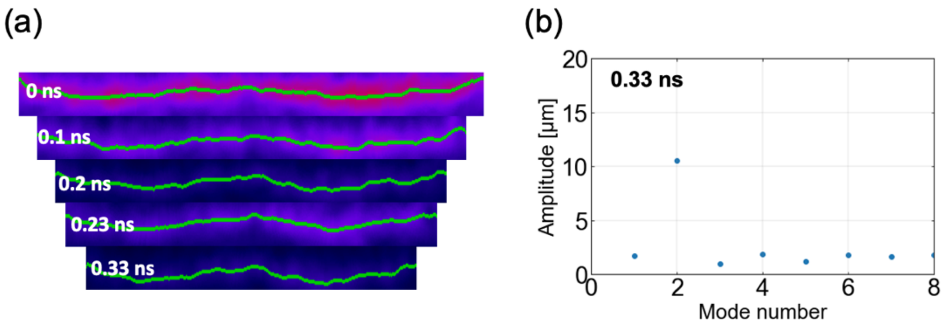

Figure 3.20. (a) Result of polar transformation of the XFC image, (b) Mode amplitudes at 0.33 ns.

Fig. 3.21 shows the time evolution of the amplitude of mode 2, where we can see a growing tendency of nonuniformity. The error bar was evaluated based on the deviation from the ideal cosine function. The cause of this experimental implosion non-uniformity is discussed later, with the radiation hydrodynamic simulation calculations.

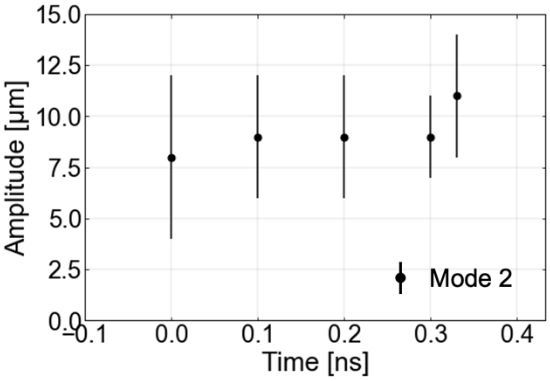

Figure 3.21. Amplitudes of mode 2 at different times.

Fig. 3.22 shows the XPHC1 image. Because XPHC integrates X-rays over the implosion, the data contains all the information over the entire implosion, both in scale and time. In the image, X-ray emissions from the resin and stalk are also observed, and the strongest emissions are located at the capsule center, which verifies the overall success of the implosion. This is unlike in the previous experiment, where abnormal X-ray emissions were observed at the side of the capsule owing to line X-rays of Si residuals. It should be noted that the XPHC2 image also showed the successful implosion of nanocrystalline diamond capsules.

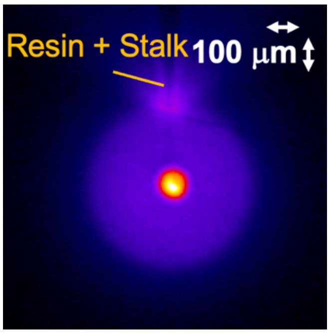

Figure 3.22. XPHC image.

3.5.4. Comparison with Radiation Hydrodynamic Simulation

The capsule trajectories from X-ray diagnostics were compared with one-dimensional radiation hydrodynamic simulations (ILESTA-1D [70]). Fig. 3.23 shows the simulation results by comparing the experimental implosion trajectories obtained from the x-ray diagnostics.

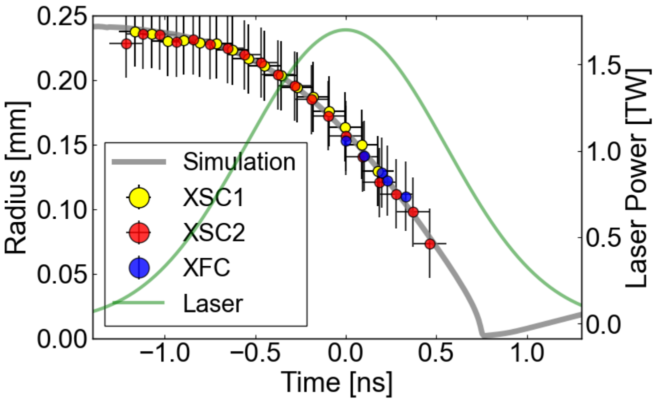

Figure 3.23. Implosion trajectories from one-dimensional simulation (ILESTA-1D) and experimental results.

The green line shows the laser intensity, and the gray line represents the implosion trajectory from the simulation. The yellow, red, and blue plots represent the experimental capsule trajectories from XSC1, XSC2, and XFC, respectively. The trajectory from the XFC was evaluated by averaging the radii over angles. The experimental results were precisely reproduced by radiation hydrodynamic simulation calculations, indicating the accurate characterization of the density and thickness of the nanocrystalline diamond capsules.

The cause of the nonuniformity of mode 2 observed in the XFC image is investigated here. In the experiment, there was a laser nonuniformity. Fig. 3.24 (a) shows an experimental laser non-uniformity in the direction of implosion non-uniformity of mode 2, where the peak and valley of mode 2 are described as “Fast” and “Slow”, respectively. The laser energy in each position is assumed as the sum of two laser beams nearest to each position, and the phase was ~22° throughout the implosion. Note that actual laser energy subjected to upper “Slow” place was smaller than the calculated value shown in

Fig. 3.24 (a) since laser light was lost at the resin and stalk. The laser energy of the "Fast" places is reasonably higher than that of "Slow" places, implying that laser nonuniformity might produce implosion nonuniformity in mode 2. For investigating laser non-uniformity effects on implosion, two-dimensional radiation hydrodynamic simulation code (PINOCO) [71] calculations were performed, assuming three cases of laser non-uniformity (5%, 10%, and 15%). Fig. 3.24 (b) shows the simulation results and experimental non-uniformity of the XFC. Experimental results were well reproduced by simulation of 10% laser non-uniformity, showing experimental non-uniformity can be reasonably attributed to the laser non-uniformity of GEKKO beams.

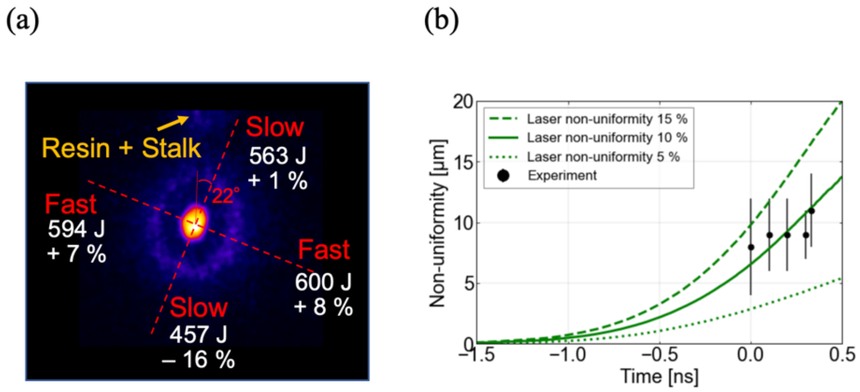

Figure 3.24. (a) Sketch of laser non-uniformity at the position of implosion non-uniformity of mode 2. "Fast" indicates the place of fast implosion, and "Slow" indicates the place of slow implosion. Laser energy and its ratio are also shown. (b) Simulated implosion non-uniformity assuming three cases of laser non-uniformity with the comparison as experimental results.

3.6. Summary and future prospects

Diamond is an attractive target material in direct-drive ICF, which can mitigate laser imprinting thanks to its stiffness and higher density than conventional capsule materials. This chapter focused on the fabrication of diamond capsules using HF-CVD technique. HF-CVD is an ideal method that can be applied to mass production. However, there were technical issues with the fabrication process. Also, the comprehensive characterization of fabricated capsules was not performed in previous works. Therefore, their applicability to actual laser experiments was unknown. In this study, experimental conditions (vibration rate of the stage and CH_4 concentration of source gases) were optimized to deposit uniform nanocrystalline diamond over Si spheres to obtain better quality capsules by HF-CVD process. Also, the etching process of the Si substrate was improved; the diamond sphere was stuck on the bottom of the beaker by clay so as not to rise onto the solution surface during etching, and the clay was removed after the etching process by acetone. Also, ultrasonic vibration was introduced to exert external pressure to overcome high surface tension at the small hole. Next, important parameters of capsules for direct-drive ICF application were evaluated. An optical microscope that employed a telecentric lens was developed to obtain an ideal backlight image of the sphere, and the average radius was evaluated by image data analysis with 0.1 μm accuracy. By using this system, a thickness was evaluated from the radius difference before and after diamond deposition. By changing the deposition duration, it was shown that capsule thickness can be controlled. Density was evaluated by electronic balance measurement, obtaining 3.2 g/cm^3. Surface roughness was evaluated to be several 10 nm by SEM and AFM, and H and W incorporation was revealed to be 1.2 at. % and 0.017 at. %, respectively. The Raman spectrum indicated the existence of sp^2 content, which reasonably explained lower density than single crystal diamond (3.5 g/cm^3). Then, the characterized diamond capsules were introduced into laser irradiation experiments to verify the quality of diamond capsules and the characterization accuracy. In the experiment, the implosion dynamic was evaluated by X-ray streak cameras, an X-ray framing camera, and X-ray pinhole cameras, and the successful implosion was observed, different from the previous experiments where significant non-uniformity and abnormal X-ray emissions due to Si residuals were observed. Experimental implosion trajectories were also compared with radiation hydrodynamic simulation calculations, which showed good agreement within the error bars. These results revealed that diamond capsules can be fabricated in a process that applies to mass production for future power generation. These results will inspire further experimental work to improve the quality of diamond capsules in this process. For example, surface roughness could be reduced by depositing ultra-nanocrystalline diamond whose grain sizes are less than 10 nm. Also, dome-shaped hills observed in the SEM image could be suppressed by changing the Mo stage into other materials where the diamond is not deposited.

4. Experimental study on laser-plasma interactions and hot electron generation

4.1. Physics of laser-plasma interactions

4.1.1. Collisional absorption

Laser energy absorption in a plasma is a fundamental phenomenon in ICF. In a laser-ablated plasma, a laser light can penetrate up to a critical density point and is mainly absorbed through collisional absorption (alias: inverse bremsstrahlung). Collisional absorption is the process where the kinetic energy of oscillating electrons due to electric fields is transferred to thermal energy by colliding with an ion and another electron. The absorption rate η_{ab} can be derived when assuming a liner density profile [72].

$$\eta_{ab} = 1 - \exp\left(-\frac{32}{15}\frac{\nu_{ei}(n_c)L_n}{c}\right) \tag{4.1}$$

$$\nu_{ei} = 3 \times 10^{-6}\frac{n_c Z ln A}{T_e^{\frac{3}{2}}[eV]} \tag{4.2}$$

Where ν_{ei} and L_n are a collisional frequency and a plasma density scale length, respectively. T_e increases with increasing laser intensity, and n_c decreases with increasing laser wavelength, which leads to the decrease of ν_{ei}. Therefore, the absorption rate becomes low in high-intensity and long-wavelength lasers. In fact, according to experimental work for a low Z ablator, an absorption rate with 351 nm laser was evaluated to be ~90 % for 10^{14} W/cm^2 and ~70 % for 10^{15} W/cm^2 while those for 527 nm laser was ~80 % for 10^{14} W/cm^2 and ~50 % for 10^{15} W/cm^2 [73].

4.1.2. Parametric instabilities

When laser intensity becomes high (typically more than several 10^{14} W/cm^2), parametric instabilities start to occur. Parametric instabilities are wave-wave interactions that involve unstable growth of multiple waves (electromagnetic waves, Langmuir waves, and ion-acoustic waves) [74]. Plasma waves driven by oscillators x_1 and x_2 and a pump wave E can be described by

$$\left[\frac{d^2}{dt^2} + \omega_0^2\right] E(t) = 0 \tag{4.3}$$

$$\left[\frac{d^2}{dt^2} + \omega_1^2\right] x_1(t) = C_1 x_2 E \tag{4.4}$$

$$\left[\frac{d^2}{dt^2} + \omega_2^2\right] x_2(t) = C_2 x_1 E \tag{4.5}$$

Where ω_1 and ω_2 are characteristic frequencies, and C_1 and C_2 depict the strength of the coupling. Here, the damping of waves is ignored. From (4.3), the pump wave can be described by

$$E = E_0 \cos(\omega_0 t) \tag{4.6}$$

By taking the Fourier transform of Eq. (4.4),

$$(\omega_1^2 - \omega^2)\hat{x}_1(\omega) = \frac{C_1 E_0}{2}[\hat{x}_2(\omega + \omega_0) + \hat{x}_2(\omega - \omega_0)] \tag{4.7}$$

From this, $x_1(\omega)$ can be coupled to oscillator $x_2(\omega \pm \omega_0)$ through a pump wave E. Here, $\hat{x}(\omega) = 1/2\pi \int x(t)\exp(i\omega t)dt$. By considering $\omega \pm \omega_0$ of oscillator x_2 and taking the

Fourier transform of Eq. (4.5),

$$(\omega_2^2 - (\omega \pm \omega_0)^2)\hat{x}_2(\omega \pm \omega_0) = \frac{C_2E_0}{2}[\hat{x}_1(\omega \pm 2\omega_0) + \hat{x}_1(\omega)] \tag{4.8}$$

$x_2(\omega \pm \omega_0)$ can feed back to the oscillation $x_1(\omega)$. Here term $\hat{x}_1(\omega \pm 2\omega_0)$ is ignored because we are looking for solutions for $\omega{\sim}\omega_1$. As a result, Eq. (4.9) is obtained.

$$\begin{pmatrix} \omega^2 - \omega_1^2 & \frac{C_1E_0}{2} & \frac{C_1E_0}{2} \\ \frac{C_2E_0}{2} & (\omega - \omega_0)^2 - \omega_2^2 & 0 \\ \frac{C_2E_0}{2} & 0 & (\omega + \omega_0)^2 - \omega_2^2 \end{pmatrix} \begin{pmatrix} \hat{x}_1(\omega) \\ \hat{x}_2(\omega - \omega_0) \\ \hat{x}_2(\omega + \omega_0) \end{pmatrix} \tag{4.9}$$

For a non-trivial solution of Eq. (4.9), the determinant must be zero. Defining $D_n(\omega) = \omega^2 - \omega_n^2$, the solutions were found by

$$D_1(\omega) = \frac{C_1C_2E_0^2}{4}\left[\frac{1}{D_2(\omega - \omega_0)} + \frac{1}{D_2(\omega + \omega_0)}\right] \tag{4.10}$$

The solution $\omega = x + yi$ with $y > 0$ indicates the instability growth and its growth rate is y. Here, we are looking for the parametric instabilities involving a laser decaying into two waves, requiring a higher frequency pump wave to decay lower frequency waves. Then, frequency $\omega + \omega_0$ can be neglected, obtaining

$$\omega_0 = \omega_1 + \omega_2 \tag{4.11}$$

This is called frequency matching conditions. A similar equation can be found in wavevector.

$$\boldsymbol{k}_0 = \boldsymbol{k}_1 + \boldsymbol{k}_2 \tag{4.12}$$

In this dissertation, as important parametric instabilities, stimulated Raman scattering (SRS) [72], where laser light decays into an electromagnetic wave (EMW) and a Langmuir wave (LW) and two plasmon decay (TPD) [72] where laser light decays into two LWs are discussed. The dispersion relation of each wave is described by

$$\omega_0^2 = \omega_{pe}^2 + c^2 k_0^2 \tag{4.13}$$

$$\omega_s^2 = \omega_{pe}^2 + c^2 k_s^2 \tag{4.14}$$

$$\omega_{LW}^2 = \omega_{pe}^2 + 3V_{th}^2 k_{LW}^2 \tag{4.15}$$

Where s indicates EMW (i.e., scattered wave). ω_{pe}, c [cm/s], and V_{th} [cm/s] are a plasma frequency, the speed of light, and a thermal velocity, respectively, and ω_{pe} and V_{th} can be described by

$$\omega_{pe} = \left(\frac{4\pi n_e e^2}{m_e}\right)^{\frac{1}{2}} \tag{4.16}$$

$$V_{th} = \left(\frac{T_e}{m_e}\right)^{\frac{1}{2}} \tag{4.17}$$

Where n_e [/cm^3], e [esu], m_e [g], and T_e [erg] are a plasma density, the elementary charge, the electron mass, and temperature. Please note that CGS unit is employed here. LWs generated by SRS and TPD lead HE generation, whose energy can be scaled by the phase velocity of LWs v_{ph}.

$$E = \frac{m_e v_{ph}^2}{2} \tag{4.18}$$

It should be noted that electrons can be accelerated through multiple LWs; Therefore, HEs of higher energy than phase velocity are also produced.

4.1.3. Stimulated Raman scattering (SRS)

In SRS, laser light decays to an electromagnetic wave (EMW) and a LW with energy and momentum conservation.

$$\omega_L = \omega_s + \omega_{LW} \tag{4.19}$$

$$\boldsymbol{k}_L = \boldsymbol{k}_s + \boldsymbol{k}_{LW} \tag{4.20}$$

An example sketch of the conservation of frequency and wavevector for SRS is shown by drawing the dispersion relation of each wave one-dimensionally in Fig. 4.1.

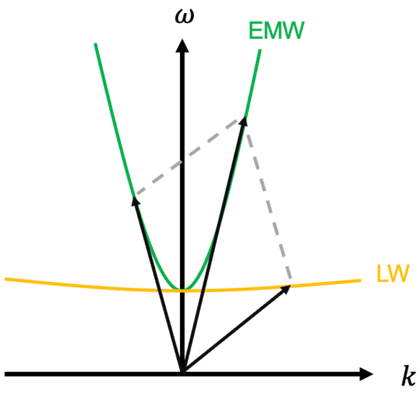

Figure 4.1. Dispersion relation of SRS.

SRS can only occur below the quarter critical density region. From Eq. (4.14), (4.15), and (4.19), the relation of frequencies is obtained.

$$\omega_0 = \omega_s + \omega_{LW} > 2\omega_{pe} \tag{4.21}$$

According to Eq. (4.16), a ratio of plasma density and critical density can be described by ω_{pe}^2/ω_0^2; Therefore, the density range where SRS can occur is calculated.

$$0 < n_{SRS} < \frac{1}{4} n_c \tag{4.22}$$

The growth rate of SRS can be calculated based on Eq. (4.10) [72], obtaining

$$\gamma = \frac{1}{4} k_{LW} v_{os} \left(\frac{\omega_{pe}^2}{\omega_s \omega_{LW}} \right)^{\frac{1}{2}} \tag{4.23}$$

Where $v_{os} = eE_0/m_e\omega_0$ is the quiver velocity of an electron. The growth rate becomes the maximum for the case of backscattering through k_{LW}, and therefore only the backscattering case is discussed in this dissertation. An instability threshold can be given considering wave damping of a scattered light and LW: ν_s and ν_{LW}.

$$\gamma^2 > \nu_s \nu_{LW} \tag{4.24}$$

This threshold intensity is easily satisfied, and in an inhomogeneous plasma, the threshold of SRS is typically given by inhomogeneity of plasma rather than Eq. (4.24). In inhomogeneous plasma, local dispersion relations for the waves depend on plasma density. Therefore, the wave number matching term $\kappa(z) = k_0(z) - k_s(z) - k_{LW}(z)$ varies with wave propagation in plasma. The perfect resonance is seen at $\kappa(z) = 0$, and SRS can be amplified until daughter waves convect away from the resonance region. When assuming the pump wave is uniform, the coupled equations can be obtained.

$$\left[\frac{\partial}{\partial t} - v_{gS}\frac{\partial}{\partial z}\right] a_S = \gamma_0 a_{LW} exp\left(i\int^{z}\kappa(z')dz'\right) \tag{4.25}$$

$$\left[\frac{\partial}{\partial t} - v_{gLW}\frac{\partial}{\partial z}\right] a_{LW} = \gamma_0 a_S exp\left(i\int^{z}\kappa(z')dz'\right) \tag{4.26}$$

v_{gS} and v_{gLW} are group velocities for a scattered light and a LW. The integral term on the right-hand side indicates the de-phasing of the resonance. Considering $\kappa(z) = \kappa' z$, so-called Rosenbluth gain that depicts spatial amplification of the instability is derived [75], which is called convective SRS.

$$G_{SRS} = \frac{2\pi\gamma^2}{\kappa'\left|v_{gs}v_{gLW}\right|} \tag{4.27}$$

Here, the thermal noise in a plasma is amplified by $I = I_0 \exp(G)$, and $G_{SRS} = 2\pi$ (i.e., $\gamma^2/\kappa'\left|v_{gs}v_{gLW}\right| = 1$) is typically used as a threshold. This conclusion is practically understood by introducing a resonance length, assuming that the resonance is lost at $\kappa(z) > 1/2$ [72].

$$\int_0^{l_{int}} \kappa\, dz = \frac{1}{2} \tag{4.28}$$

Therefore, the resonance length is obtained as $l_{int} = 1/\sqrt{\kappa'}$. It can be regarded that the wave convects away from this resonance length with damping rate $\nu_{S*} = v_{gS}/l_{int}$ and $\nu_{LW*} = v_{gLW}/l_{int}$. Therefore, the instability threshold given by $\gamma^2 > \nu_{s*}\nu_{LW*}$, is calculated to $\gamma^2/\kappa'\left|v_{gs}v_{gLW}\right|$. It should be noted that when the density is very close to $n_c/4$, v_{gs} approaches zero, and convective SRS cannot occur. Instead, absolute SRS could occur, which is amplified not spatially but temporarily at $n_c/4$ [76].

The general form of Eq. (4.27) can be more specific by substituting $v_{gs} = k_s c^2/\omega_s$ and $v_{gLW} = 3k_{LW}V_{th}^2/\omega_{LW}$ and calculating $\kappa'(z)$ [77],

$$G_{SRS} = \frac{2\pi}{8}\left(\frac{v_{os}}{c}\right)^2 \frac{k_{LW}^2}{\left|k_{LW} - k_0\right|} L_n \propto I L_n \tag{4.29}$$

Because $v_{os}^2 \propto I$, a convective gain of SRS is proportional to a laser intensity and a density scale length.

4.1.4. Two plasmon decay (TPD)

In TPD, laser light decays into two LWs with energy and momentum conservation.

$$\omega_0 = \omega_{LW1} + \omega_{LW2} \tag{4.30}$$

$$\boldsymbol{k}_0 = \boldsymbol{k}_{LW1} + \boldsymbol{k}_{LW2} \tag{4.31}$$

An example sketch of the conservation of frequency and wavevector for TPD is shown by drawing the dispersion relation of each wave one-dimensionally in Fig. 4.2.

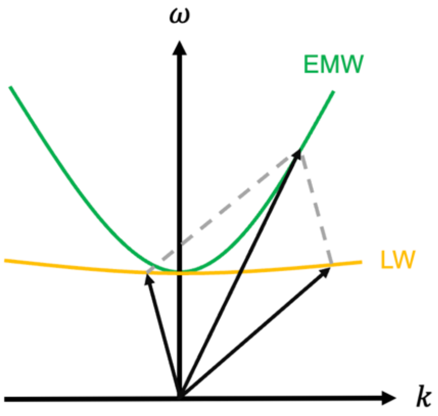

Figure 4.2. Dispersion relation of TPD.

Because frequency of a LW is close to plasma frequency ω_{pe},

$$\omega_0 = \omega_{LW1} + \omega_{LW2} \sim 2\omega_{pe} \tag{4.32}$$

This means that TPD occurs at around a quarter-critical density. In more detail, because the dispersion relation of LWs has a term of $3V_{th}^2 k_{LW}^2$, ω_{LW1}, and ω_{LW2} shift from $\omega_0/2$, higher frequency ω_{UE} and lower frequency ω_{DE}. The growth rate of TPD is also calculated by dispersion relation [72].

$$\gamma = \frac{\boldsymbol{k}_{LW} \cdot \boldsymbol{v}_{os}}{4} \left| \frac{(\boldsymbol{k}_{LW} - \boldsymbol{k}_0)^2 - k_{LW}^2}{k_{LW} |\boldsymbol{k}_{LW} - \boldsymbol{k}_0|} \right| \tag{4.33}$$

Similarly, Rosenbluth gain for convective TPD can be derived when $v_{th} \ll c$ [77],

$$G_{TPD} = \frac{2\pi}{24} \left(\frac{v_{os}}{v_{th}} \right)^2 k_0 L_n \propto I L_n / T_e \tag{4.34}$$

The gain of convective TPD is proportional to laser intensity and a plasma density scale length. Also, it is inversely proportional to plasma temperature because of $v_{th}^2 \propto T_e$.

4.2 Significance of this study

As mentioned in the previous chapter, HEs could be detrimental or beneficial in direct-drive ICF. For example, in SI scheme, HEs degrade implosion performance due to fuel preheating in the compression phase. In contrast, they are expected to contribute to ablation pressure formation in the ignition phase. From the above, it is essential to understand the occurrence of SRS, TPD, and HE generation. In inhomogeneous plasma, their extent is depicted by Rosenbluth gain by considering a finite resonance length, as shown above. However, it is known that plasma waves are subjected to damping due to multiple factors, which also could suppress their growth. Such saturation due to the damping of LWs was explored in detail in homogeneous plasma in indirect-drive ICF conditions. It was found that ion-acoustic wave (IAW) damping is an important factor for

SRS saturation through damping of LWs due to Langmuir decay instability (LDI) [78–84], showing that plasma composition is important to control their occurrence [79,84,85]. On the other hand, it was unknown whether those damping also determines the level of SRS and TPD in direct-drive ICF conditions, making it difficult to anticipate the extent of SRS, TPD, and HEs in direct-drive ICF conditions; there is only a limited number of works that explored the effects of plasma composition on the levels of SRS and TPD in direct-drive ICF conditions where different saturation mechanisms were discussed [49,86,87]. From the above, it was important to experimentally explore the extent of SRS, TPD, and HEs in direct-drive conditions and discuss their saturation mechanisms. Here the experimental platform which enables to characterize SRS, TPD, and HEs was developed at the GEKKO laser facility (Section 4.4), and the SRS, TPD, and HEs were comprehensively characterized in detail for plastic targets, which is the most typical ablator material (Section 4.5). Then, the diamond ablator's SRS, TPD, and HEs were explored and compared to plastic (Section 4.6). This study's results and discussion provided detailed information on the extent of SRS, TPD, and HEs. Also, from the comparison of diamond and plastic targets, H effects in the ablator material on the saturation of SRS and TPD through IAW damping were revealed. This finding will contribute to the design of ICF target to improve the implosion performance.

4.3. Experimental conditions

An experimental platform was established at Chamber II at the GEKKO laser facility, called "GEKKO-HIPER", where twelve laser beams (*f/15*) are combined into one *f/3* laser bundle. In the experiments, seven frequency-tripled laser beams (3ω, I~2.2×10^{15} W/cm^2)

with a Gaussian temporal profile (full width at half maximum (FWHM)=230 ps), delivering an energy of 420–510 J was employed. Its spot size was 280 μm at the FWHM, providing an envelope peak intensity of 1.9–2.4×10^{15} W/cm^2. Also, three frequency-doubled beams (2ω) were used as the prepulse to produce a preformed scale-length plasma 200 ps before the main pulse. They delivered 250 J in 240 ps with a Gaussian profile and were focused on a spot of 850 μm FWHM for an intensity of 1×10^{14} W/cm^2. The 3ω and 2ω beams were mounted on random phase plates (RPP) [30] and kinoform phase plates [31], respectively. As a target, three layered targets consisting of ablator, copper (Cu), and quartz (Qz) layers were typically employed, as shown in Fig. 4.3. As ablators, diamond (C) 40 μm, polystyrene (CH) 10 μm, or polyethylene (CH_2) 10 μm were employed. Cu and Qz layers were employed for X-ray diagnostics for HEs and shock parameter measurements, respectively. Table 4.1 shows the summary of laser shot conditions referred in the dissertation. Multiple diagnostics were employed to explore SRS, TPD, and HEs, and some of them were developed in this study, which are explained in the next section. The plan view of all diagnostics is shown in Fig. 4.4.

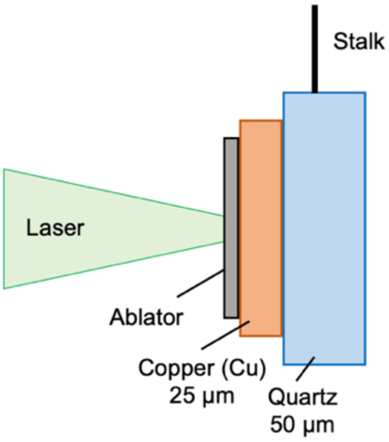

Figure 4.3 Structures of Multi-layered targets.

Table 4-1. List of laser and target conditions

#shot	Ablator	Pre-pulse intensity [10^{15} W/cm^2]	Main pulse intensity [10^{15} W/cm^2]
44690	CH_2	–	2.2
44733	CH_2	–	2.4
44681	CH_2	0.11	2.1
44682	C	0.12	2.2
44683	CH	0.10	1.9
44684	C	0.11	2.0
44685	C	0.11	2.1
44687	CH_2	0.12	2.3
44688	CH_2	0.13	2.3

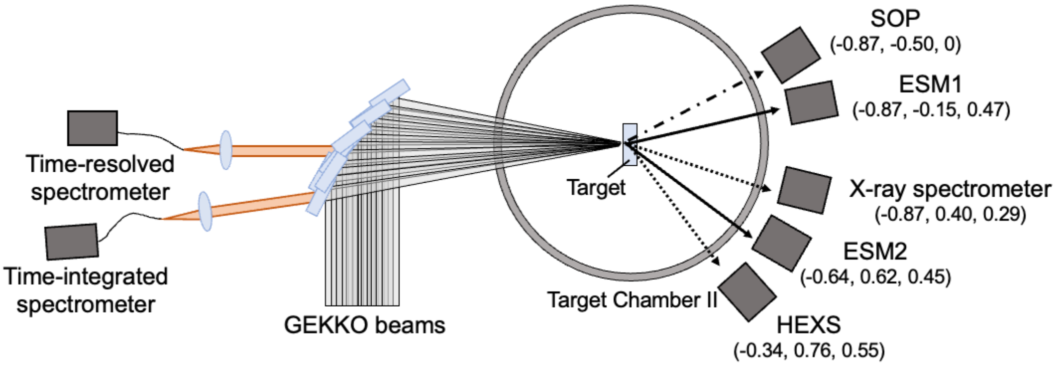

Figure 4.4. Plan view of all diagnostics. *(a, b, c)* indicates a direction cosine of the chamber port from the center of a chamber when that of the laser port is *(1, 0, 0)*.

4.4. Development of experimental platform

In this chapter, principles, typical analysis, and typical results for diagnostics are explained.

4.4.1. Backscattered optical spectrometer

Optical systems for measuring backscattered emissions were developed to evaluate the occurrence of SRS and TPD. For SRS, the wavelength of scattered light in a vacuum is calculated by

$$\lambda_s = \frac{2\pi c}{\omega_s} \tag{4.35}$$

From $1/2\,\omega_0 \lesssim \omega_s < \omega_0$, $351 < \lambda_{SRSs} \lesssim 702$ nm is obtained for $\lambda_0 = 351$ nm. For TPD, TPD itself does not produce EMWs. However, LWs generated by TPD interact with laser light, producing scattered light: $\omega_0 \pm \omega_{UE}$ and $\omega_0 \pm \omega_{DE}$ [88]. In the case of difference frequency,

$$\omega_{sB} = \omega_0 - \omega_{UE} \tag{4.36}$$

$$\omega_{sR} = \omega_0 - \omega_{DE} \tag{4.37}$$

From $\omega{\sim}\omega_{UE}{\sim}\omega_{DE}{\sim}\,1/2\,\omega_0$, $\omega_{sB}{\sim}\omega_{sR}{\sim}\,1/2\,\omega_0$, and therefore, $\lambda_{TPDs}{\sim}702$ nm. ω_{sB} and ω_{sR} are usually called “blue shift” and “red shift”, respectively.

Time-resolved and time-integrated spectrometers were arranged to obtain optical emissions from SRS and TPD. The time-resolved optical spectrometer was employed to evaluate the timing of each instability, and the time-integrated spectrometer was employed to obtain a scattered spectrum and its magnitude. Fig. 4.5 shows the developed system for the time-resolved and time-integrated spectrometers.

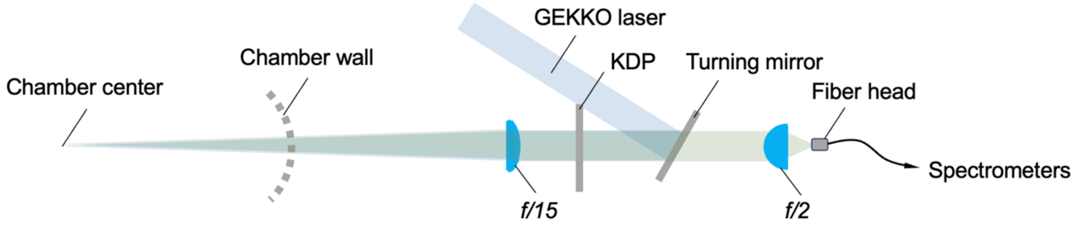

Figure 4.5. System of the time-resolved and time-integrated optical spectrometers.

The backscattered light generated at an ablation plasma from the target traveled backward along the same path as the incident laser up to the turning mirror, which only reflected λ=1053 nm light. It then passed through three optical filters: a 400 nm high-pass filter, a 527 nm notch filter, and a 1000 nm low-pass filter. Finally, a Fresnel lens focused the transmitted light into a fiber and transported it to the two spectrometers. A 1.8 m quartz fiber was employed to transport the backscattered light to the time-integrated spectrometer (OCEAN optics, HR2000), while a 20.4 m quartz fiber was employed for the time-resolved spectrometer (Hamamatsu, A6365). The spectral resolution was evaluated to be 3 nm and 2 nm for time-integrated and time-resolved spectrometers, and the sweep time window of the streak camera was 1.62 ns or 5.26 ns, leading to a time resolution of 20 ps or 50 ps. Here, the chromatic time delay in an optical fiber for the time-resolved optical spectrometer was corrected by considering a group velocity of light. The required time for light to propagates in an optical fiber is described by

$$t = L(n - \lambda\, dn/d\lambda)/c \tag{4.38}$$

where L, n, λ, and c are a cable length, a reflective index, a wavelength, and the speed of light, respectively. The reflective index n was calculated from the Malitson equation in fused quartz [89].

$$n^2 - 1 = \frac{0.6961663\lambda^2}{\lambda^2 - 0.0684043^2} + \frac{0.4079426\lambda^2}{\lambda^2 - 0.1162414^2} + \frac{0.8974794\lambda^2}{\lambda^2 - 9.896161^2} \tag{4.39}$$

Fig. 4.6 shows the result of the time-integrated spectrometer for SN 44681 as an example.

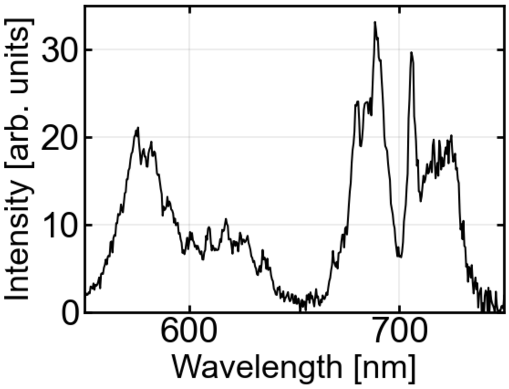

Figure 4.6. Result of the time-integrated optical spectrometer for SN 44681.

The scattered lights from 550 to 650 nm were from convective SRS [88,90,91], and half-harmonic spectra $\omega_0/2$ where blue- and red-shifted broad peaks were attributed to convective TPD [88,92], and the sharp redshifted peak close to 702 nm was attributed to hybrid absolute SRS/TPD [88]. In the following manuscript, convective SRS and convective TPD are mainly discussed. Signals from hybrid SRS/TPD were employed for an evaluation of plasma temperature by

$$\frac{\delta\omega}{\omega_0} = 2.2 \times 10^{-3} T_e \tag{4.40}$$

This equation can be obtained by considering backscattered TPD [88]. Absolute calibration of energy of backscattered SRS was performed by employing a power meter. However, stray signals were included in the measured energy. When assuming that stray signals were proportional to laser intensity, measured energy in the power meter can be described by $E_{cal} = iE_{laser} + jI_{SRS+TPD}$ where i [-] and j [J/counts]. Using the pre-pulse irradiation dataset, the optimum value of j was calculated to minimize $\sum(E_{cal} - E_{measure})^2$, obtaining 0.000719 [mJ/count]. In addition, the total transmittance rate of all the optical components from the target to a power meter was measured to be 0.15 by employing $\lambda = 660$ nm laser. These estimations enabled the evaluation of the absolute backscattered light intensity, revealing that the SRS reflectivity in SN 44681 was 0.03 %.

Fig. 4.7 shows a streaked image of the time-resolved optical spectrometer in the same shot (SN 44681). A similar spectrum with the time-integrated optical spectrometer is observed where convective SRS, convective TPD, and absolute hybrid SRS/TPD were seen. Here, it should be noted that the onset of TPD was observed earlier than SRS, which is discussed later.

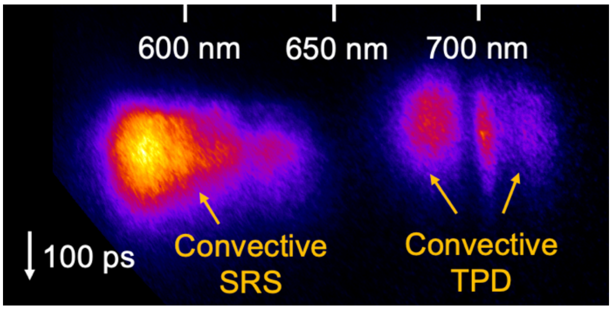

Figure 4.7. Streaked image of the time-resolved optical spectrometer for SN 44681.

4.4.2. Electron spectrometer

HE energy due to LPIs are typically in the range of 10 to 200 keV. An electron spectrometer (ESM) was developed to evaluate such HE spectra. The basic structure of ESM is shown in Fig. 4.8.

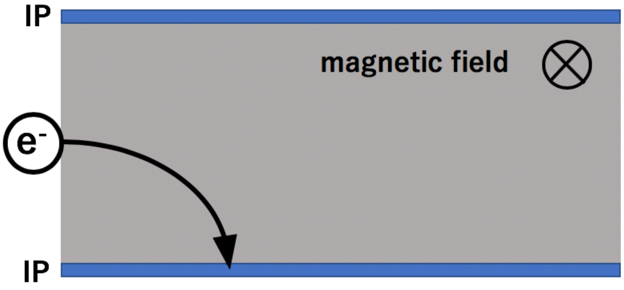

Figure 4.8. Structure of ESM.

Neodymium magnets were employed to bend electron trajectory, and electrons were detected on an imaging plate (IP). IP records (i.e., stores) the energy deposition of radioactive ways such as electrons and X-rays, and the stored energy is read as a unit of PSL in the GE scanning system. Empirical sensitivity curves of IP were known in previous works [PSL/electron, PSL/photon] [93,94]. The stored signals decrease with time, which is called fading, and therefore, the raw signal should be corrected by a fading curve in the analysis [94]. IPs were set on both sides of the ESM, as shown in Fig. 4.8; therefore, this ESM could measure both electron and ion spectra. Two ESMs were made, and the magnetic fields were measured by a magnetic probe. Measured magnetic fields were slightly different; therefore, two ESMs were named ESM1 and ESM2, respectively.

The result of the magnetic field measurement for ESM1 is shown in Fig. 4.9.

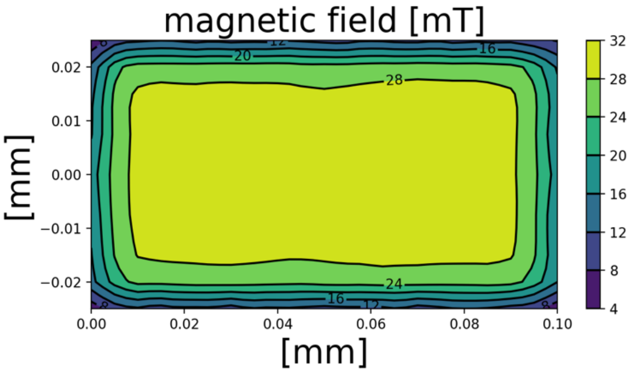

Figure 4.9. Measured magnetic field for ESM1.

Because the magnetic fields were not uniform, an electron trajectory was calculated at the local magnetic field according to its pass. For relativistic electrons, the relation of kinetic energy and its velocity can be described by

$$E_{kin} = \frac{m_0}{\sqrt{1 - \frac{v^2}{c^2}}} c^2 - m_0 c^2 \tag{4.41}$$

The equation of motion of an electron in the magnetic field B is described by

$$m\dot{v}_x = -ev_y B \tag{4.42}$$

$$m\dot{v}_y = -ev_x B \tag{4.43}$$

From Eq. (4.42) and (4.43) and by assuming initial values of velocity from Eq. (4.41), $\mathrm{d}v_x$, $\mathrm{d}v_y$, $\mathrm{d}x$, and $\mathrm{d}y$ due to $\mathrm{d}t$ were calculated in the local magnetic field values. The projected position of an electron on an IP was obtained by reiterating the calculations.

Here, the time step was set to 5 fs. The calculated results for ESM1 and ESM2 are shown in Fig. 4.10.

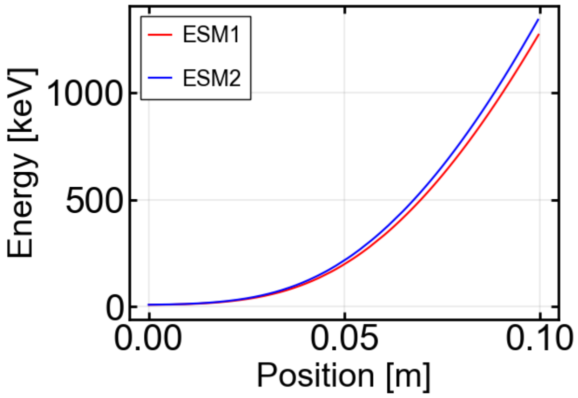

Figure 4.10. Relation of electron energy and IP position for ESM1 and ESM2.

The lowest energy for ESM1 and ESM2 was ~10 keV, and the maximum energy was ~1.3 MeV. However, low-energy electrons mainly pass through the edge of a magnetic field where they are not uniform (i.e., unreliable). Therefore, practical data for the energy range of 100 keV to 1.3 MeV was employed for their analysis. Fig. 4.11 shows the results of ESM1 and ESM2 for SN 44688. In this shot, Cu and Qz layers were not employed in the target to avoid the attenuation of HEs in those layers. In fact, HE spectra were too weak to conduct reliable analysis in other shots with the targets, including Cu and Qz layers. Slope temperature was evaluated by fitting electron spectra between 100 and 300 keV in SN 44688, obtaining 24 keV for ESM1 and 22 keV for ESM2.

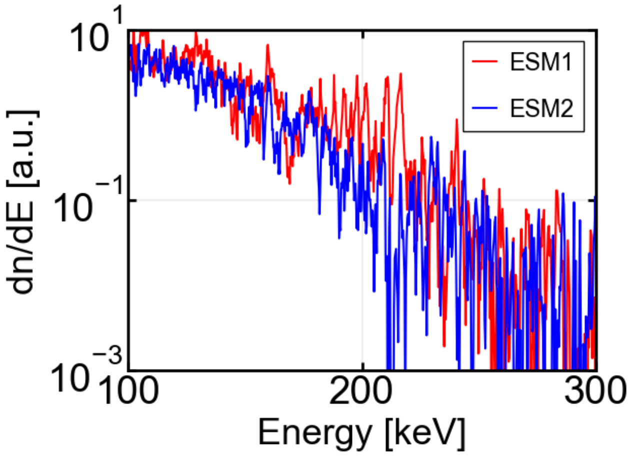

Figure 4.11. Electron spectra for ESM1 and ESM2 for SN 44688.

4.4.3. X-ray spectrometer

An X-ray spectrometer was employed to measure the Cu-Kα line to evaluate HEs. Here, a principle of the diagnostic and analyzation method are explained. When HEs hit the Cu layer, characteristic X-rays are emitted. Fig. 4.12 shows the schematic of the structure of the X-ray spectrometer. The incident X-ray is reflected on the HOPG plate at the Bragg angle and reaches the IP.

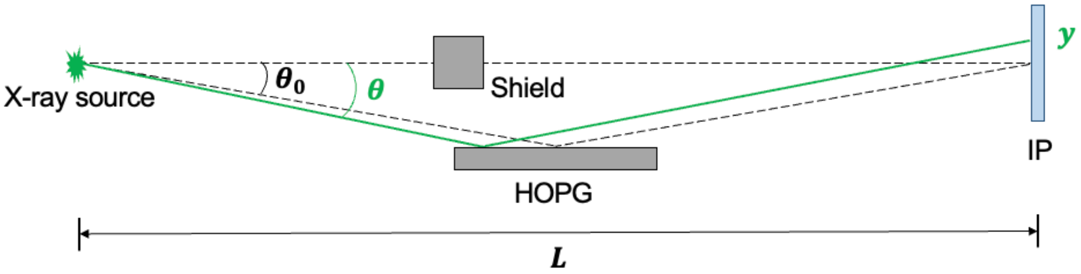

Figure 4.12. Structure of X-ray spectrometer.

A position y on the IP from its center is described by

$$y = L\tan\theta - L\tan\theta_0 \tag{4.44}$$

Applying Bragg law: $\lambda = 2d\sin\theta$ (d is a lattice spacing; Here, d was 3.3557 Å.), eq. (4.44) is rewritten by

$$\lambda = 2d\sin\left\{\tan^{-1}\left(\frac{L\tan\theta_0 + y}{L}\right)\right\} \tag{4.45}$$

Depending on the purpose of the experiment, values of θ_0 or L are chosen. In this experiment, to place the Cu-Ka line (8.04 keV, 1.542 Å) to the center of IP, θ_0 was set to 12.84 ° (Correspondingly L was 500 mm). Using two different energy lines, a relation of IP position to X-ray energies can be calculated throughout the IP. In this work, because the attentions were placed on the Cu-Kα line, the IP position only near the Cu-Kα line was calibrated by calculating dE/dy from $E = 12.4/\lambda$ [å] and Eq. (4.45). The result for SN 44681 is shown in Fig. 4.13 as an example.

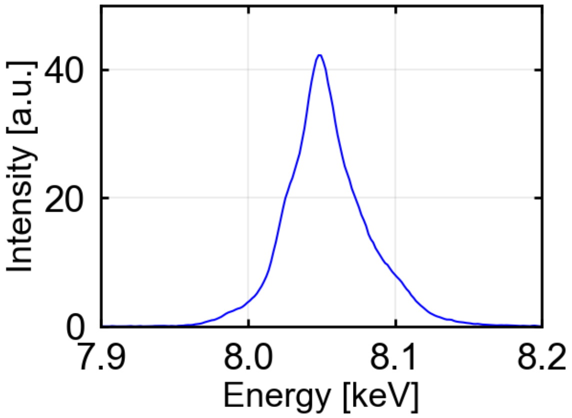

Figure 4.13. Result of X-ray spectrometer for SN 44681.

4.4.4. High energy x-ray spectrometer

A high-energy X-ray spectrometer (HEXS) [95–97] was employed to collect Bremsstrahlung continuum X-ray emissions to evaluate the HE spectrum and its fluence. Here, a principle and analysis process are explained. Fig. 4.14 shows the schematic of HEXS where interposed metal filters separate 12 IPs; the filters consisted of Al (100 μm), Ti (100 μm), Fe (100 μm), Cu (100 μm), Mo (100 μm), Ag (200 μm), Sn (500 μm), Ta (400 μm), Pb (1 mm), Pb (2 mm), Pb (3 mm), and Pb (4 mm).

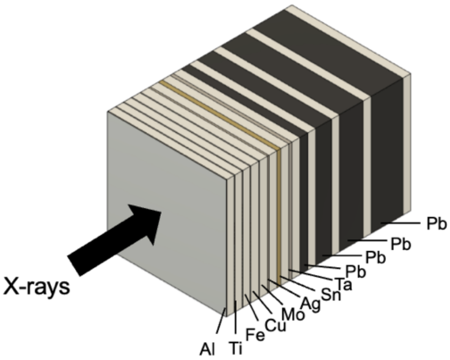

Figure 4.14. Principle of HEXS.

Because the minimum detectable X-ray energy is 10 keV, HEXS requires sufficiently high energy of X-ray signals. The analysis can deduce the electron spectrum from experimental results by comparing it with simulation. The analyzation flow is shown in Fig. 4.15.

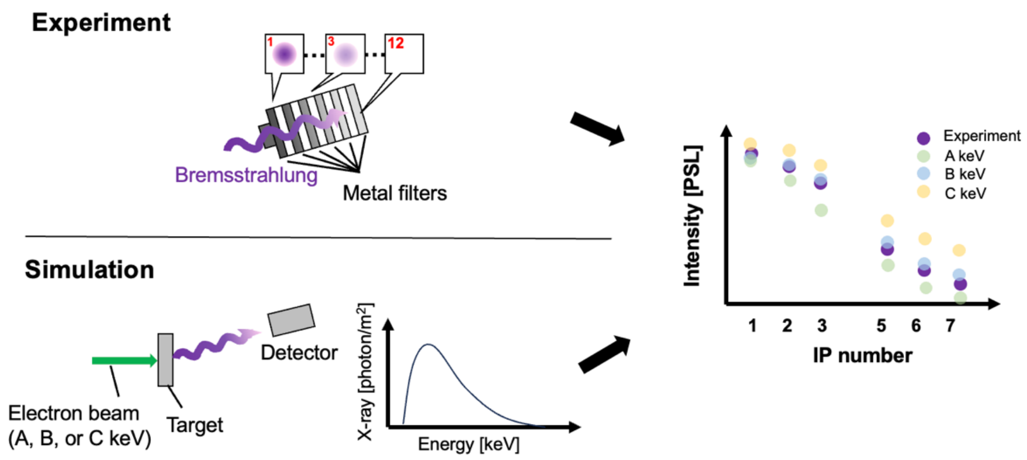

Figure 4.15. Flow for analysis of HEXS. In this figure, HE temperature was evaluated to be B keV.

Analysis for SN 44681 is shown as an example. IPs #1 to #7 were employed for the analysis because the signals of IPs #8 to #12 were too weak. Fig. 4.16 shows the dose value on each IP [PSL/pixel] after correcting the fading effects of the IPs.

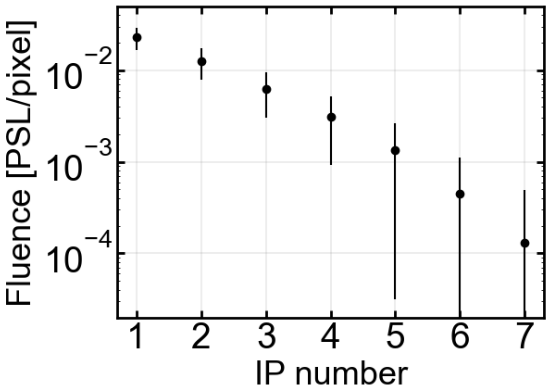

Figure 4.16. Experimental fluence on IPs for SN 44681.

In a simulation, HEs with a single Maxwellian distribution T_e was assumed, and they were injected into a target from a normal direction, and the X-ray spectrum was measured at the entrance of the HEXS. The simulation was done using the PHITS code (Particle and Heavy Ion Transport Code System) [98]. HE temperature in the simulation was chosen from 14 to 34 keV with the step of 2 keV. Also, to save simulation cost, the solid angle of HEXS entrance in the simulation was extended 392 times compared to an actual setup. Fig. 4.17 shows an example of the X-ray spectrum at the entrance of HEXS calculated in T_e=22 keV.

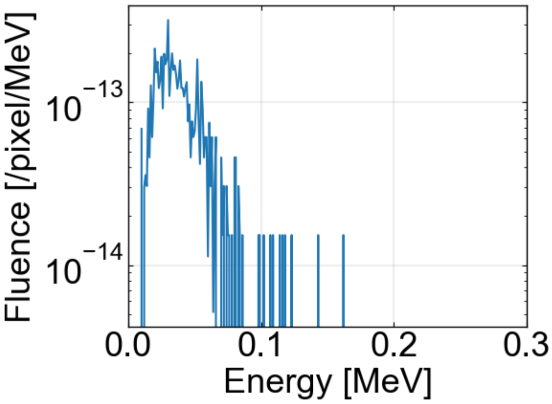

Figure 4.17. X-ray spectrum at the entrance of HEXS from simulation for T=22 keV.

Next, X-ray spectra at the HEXS entrance were converted to dose value in each IP. Here, a sensitivity curve calculated in the previous work [95], shown in Fig. 4.18, was employed.

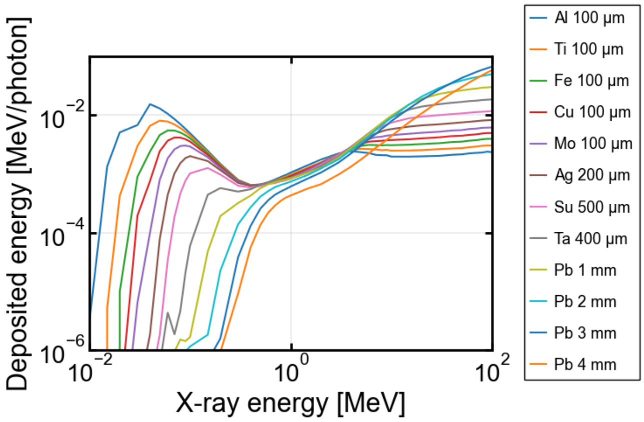

Figure 4.18. Sensitivity curve of HEXS.

As a result, deposited energies in each IP were obtained. The appropriate temperature was determined by comparing the simulation and experimental results to minimize the deviation between the experiment and simulation results. Fig. 4.19 shows the simulation results for 22 keV with the smallest deviation from the experiments. Also, by using the coefficient between PSL and MeV: 2.05 MeV/PSL [95], the absolute hot electron fluence was evaluated, and therefore the conversion rate of HE from laser energy was evaluated, obtaining 0.3 % in SN 44681.

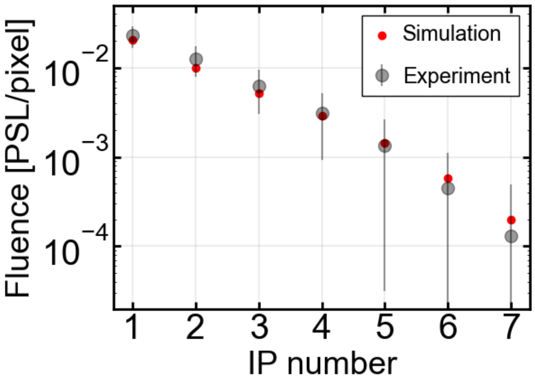

Figure 4.19. Comparison of simulation and experimental results for SN 44681.

4.4.5. Streaked optical pyrometer

In the regime where LPIs are significant, a scaling of ablation pressure based on collisional absorption and the classical ablation model that considers a constant heat flow due to thermal heat conduction is no longer valid because of loss of laser absorption due to LPIs and energy transport of HEs. Previous works implied that HEs could enhance ablation pressure. From the above, experimental measurements of ablation pressure are of great importance. In this experimental platform, the shocked temperature in the Qz layer was measured by a streaked optical pyrometer (SOP) [99]. Qz is a popular material for shock wave measurements because the hugoniot of Qz (i.e., the relation of shock velocity u_s and particle velocity u_p) is well known [100]. Also, the relation between shocked temperature and shock velocity in the Qz is studied [101]. Therefore, the shock pressure P can be obtained from the shocked temperature by [13]

$$P = \rho_0 u_p u_s \tag{4.46}$$

In the SOP system, the self-emissions from the shock front are recorded on a streak camera whose time range was set to 9.72 ns. The optical lights were transported through an image relay system, and emissions were limited to 450 nm by using bandpass filters. For analysis, temperature was evaluated by using Planck's law, which connects optical emission and the temperature of a material [99].

$$T = \frac{T_0}{ln\left(1 + \frac{1-R}{I} A\right)}, T_0 = \frac{hc}{\lambda_0}, \tag{4.47}$$

where I is the optical intensity in the SOP image, R is a reflectivity of the shock front, h is Planck's constant, c is the speed of light, λ_0 is an emission wavelength, and A is a unique constant that depends on the experimental setup. To determine A, SOP was calibrated by measuring the shock velocity by a VISAR system (velocity interferometer system for any reflector) [102], obtaining $A = 890 \pm 290$ [Appendix]. For example, the analysis results for the shocked temperature for SN 44681 are shown in Fig. 4.20.

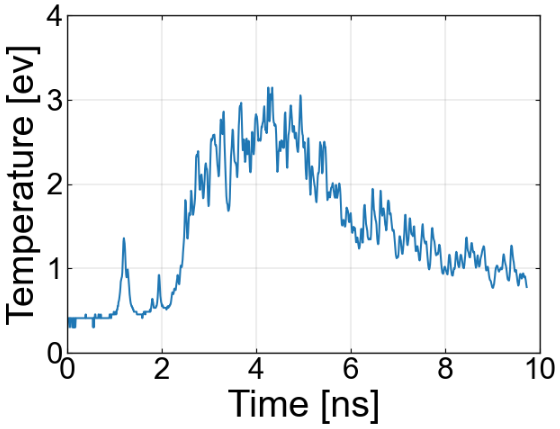

Figure 4.20. Shocked temperature from the SOP for SN 44681.

In the dataset referred in this dissertation, the ablation pressure enhancement was not observed in the SOP, and therefore, SOP was not discussed in the following manuscript. In this dataset, the dominant source of HEs was TPD, whose divergence angle is large (close to 45 degrees), and laser intensity was not high enough to produce a high flux of HEs (around 0.3 %). Therefore, an ablation pressure enhancement was not observed. The details of characterization of LPIs and HEs are shown later in greater detail.

4.4.6. Consistency of diagnostics

The experimental results were compared to verify the consistency of measuring instruments. The results of the time-integrated spectrometer and the integrated spectrum of the time-resolved spectrometer were compared for SN 44681 in Fig. 4.21. The spectra were normalized at ~580 nm.

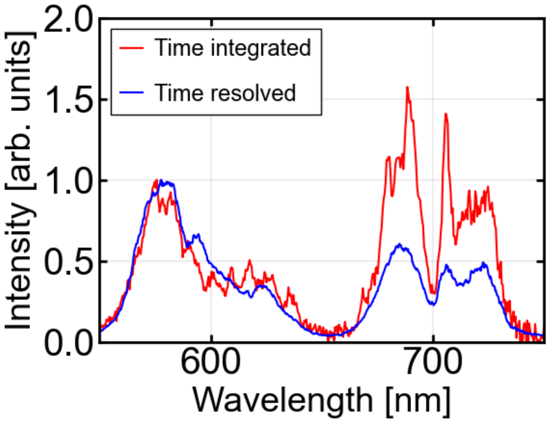

Figure 4.21. Comparison of time-resolved and time-integrated spectrometer for SN 44681.

The basic features of spectra are the same as expected. However, the relative intensity of those spectra differed in wavelength. This could be explained by color aberration due to the Fresnel lens. A slight deviation from the focusing lens position makes a difference. For accurate calibration, it is ideal to introduce an integrated sphere before the time-integrated spectrometer in the future.

The consistency of diagnostics for HE characterization was also confirmed. The X-ray spectrometer and HEXS should be correlated with each other. Fig. 4.22 compares the absolute number of HEs from the HEXS and integrated intensity from the X-ray spectrometer for the CH_2 target.

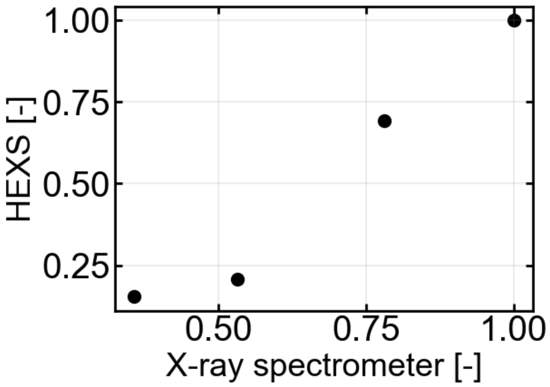

Figure 4.22. Comparison of HEXS and X-ray spectrometer for CH_2 targets.

The number of HEs from the HEXS increased with increasing Cu-Kα intensity from the X-ray spectrometer, showing a reasonable tendency. ESM should also be correlated with HEXS. In SN 44688, the slope temperature was evaluated as 24 keV for ESM1 and 22 keV for ESM2. For HEXS, the temperatures of HEs were evaluated in the range of 20 to 22 keV in the CH_2 target for all the shots, which show reasonable agreement with each other.

4.5. Characterization of SRS, TPD, and hot electrons

This chapter discusses the experiential results for CH_2 targets to understand the details of SRS, TPD, and HEs in this dataset.

4.5.1. Effects of pre-pulse irradiation

Fig. 4.23 compares without pre-pulse irradiation (SN 44690) and pre-pulse irradiation (SN 44687). In pre-pulse irradiation, SRS and TPD become significant, although the main laser intensity in SN 44687 was lower than that of SN 44690. This can be explained by considering Rosenbluth gain factor. Rosenbluth gain factors of SRS and TPD have simple relations $G_{SRS} \propto IL_n$ and $G_{TPD} \propto IL_n/T_e$, indicating that SRS and TPD become significant with longer density scale length. With pre-pulse irradiation, the plasma scale length was extended, which led to an increased gain of SRS and TPD. This verified that SRS and TPD in this dataset can be described by Rosenbluth gain, which considers plasma inhomogeneity in direct-drive ICF conditions.

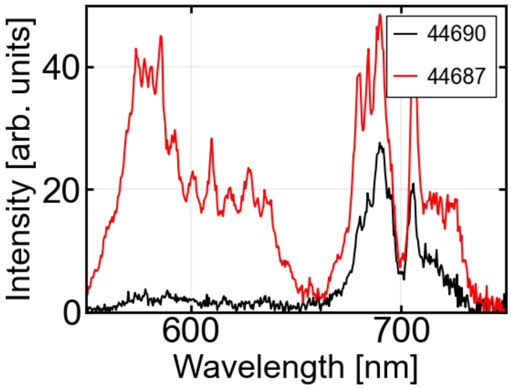

Figure 4.23. Comparison of the time-integrated spectrometer without and with pre-pulse irradiation (W/o SN 44690 and W/ SN 44687).

4.5.2. Dependence of laser intensity

The dependence of SRS and TPD on different laser intensities was discussed to understand SRS and TPD further. Fig. 4.24 shows the result of the time-integrated backscattered spectra for SN 44681 (2.1×10^{15} W/cm^2) and SN 44688 (2.3×10^{15} W/cm^2).

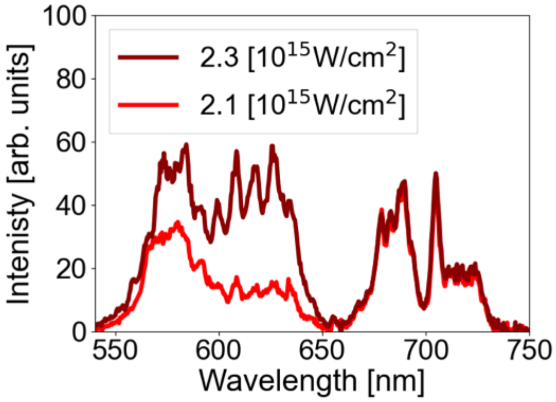

Figure 4.24. The results of time-integrated spectrometer in different laser intensity.

When the laser intensity slightly increased by ~10 %, the spectrally integrated SRS light intensity (λ=560–640 nm) increased by a factor of 2.3, whereas that of TPD (λ=650–700 nm) remained virtually the same.

One-dimensional radiation-hydrodynamic simulations (ILESTA-1D) were performed to estimate the plasma conditions, such as electron temperature and a plasma density scale length, to understand experimental conditions. The electron temperature at $0.25n_c$ (n_c: critical density for λ=351 nm) was also evaluated from a red-shifted sharp peak at ~702 nm using Eq. 4.40 [88]. Data from the time-resolved optical spectrometer were used for the evaluation. Fig. 4.25 shows the evaluated peak electron temperature and the corresponding simulation results at $0.25n_c$ in all shots in the dataset with pre-pulse irradiation.

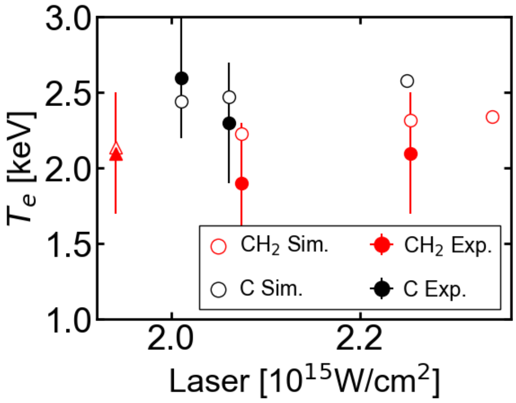

Figure 4.25. Comparison of plasma temperature between simulation and experiment.

Note that the triangle plot refers to the results of a shot on a polystyrene (CH) target. Temperatures evaluated from the experimental data generally demonstrated acceptable agreement with the simulation results, verifying the validity of the simulation.

By using the electron temperature and plasma scale length from the simulation, a density n_e and parameter $k_{LW}\lambda_D$ (k_{LW}: LW wavenumber, λ_D: Debye length) for SRS and TPD were evaluated [90]. The value of $k_{LW}\lambda_D$ is typically considered a marker for assessing the significance of Landau damping. Typically, when $k_{LW}\lambda_D$ is greater than 0.3, kinetic effects due to trapping of HEs become important. In such cases, electron distribution could differ, and frequency shifts of LWs could occur [103–107]. For SRS, by assuming a plasma density and the temperature, parameters of the dispersion relation of each wave can be calculated by using Eq. (4.13) – (4.15), (4.19), and (4.20) for the case of backscattering. That means that a plasma density and a wavenumber of each wave can be obtained from the measured backscattered light (i.e., a frequency) when assuming a plasma temperature. For TPD, obtaining parameters of the dispersion relation is not as straightforward as SRS. The frequency shift of scattered light $\Delta\omega_{TPD}$ is described from Eq. (4.15)

$$\Delta\omega = \omega_{UE} - \omega_{DE} = \frac{3v_{th}^2(k_{UE}^2 - k_{DE}^2)}{\omega_0}$$
$$\therefore \frac{|\Delta\omega_{TPD}|}{\omega_0} = \frac{\Delta\omega}{2\omega_0} = \frac{9}{4}v_{th}^2\frac{1}{c^2}\left(\frac{k_{UE\parallel}\,k_0}{k_0^2} - \frac{1}{2}\right) \tag{4.48}$$

This means that $k_{UE\parallel}$ is obtained from a frequency shift. Here $\parallel$ indicates that parallel to the incident laser light. As mentioned in the section above, LWs that meet hyperbola have the highest growth rate [90].

$$k_{UE\perp}^2 = k_{UE\parallel}(k_{UE\parallel} - k_0) \tag{4.49}$$

Therefore, $\boldsymbol{k}_{UE}$ is obtained. As a result, from an experimentally measured frequency shift, plasma density and a wavenumber of each wave can also be obtained by Eq. (4.13) – (4.15), (4.30), (4.31), (4.48), and (4.49). For SN 44681 and 44688, shown in Fig. 4.24, the shapes of backscattered spectra were comparable, and n_e and $k\lambda_D$ were calculated for the emission in the range of 560–640 nm for convective SRS, obtaining n_e=0.11–0.19 n_c and $k\lambda_D$=0.28–0.19. The peak emission was at ~580 nm, corresponding to 0.13 n_c and $k\lambda_D = 0.26$. For convective TPD, peak emission at 690 nm corresponded to n_e=0.23n_c and $k\lambda_D$=0.19. Because the values of $k\lambda_D$ are smaller than 0.3, kinetic effects should not be dominant in this condition. Also, from Eq. (4.29) and (4.34), Rosenbluth gain for convective SRS and TPD were calculated at peak emission points. For SN 44681 and SN 44688, G_{SRS} was evaluated to be 0.80 and 0.95, respectively, and G_{TPD} was 11.1, and 12.2, respectively. This means that SRS is below the threshold whereas TPD is above the threshold when considering the threshold as 2π. This suggests that convective SRS occurred only in local higher-intensity regions produced by RPP speckles [108], the superposition among the beams, and the subsequent self-focusing [47]. Therefore, SRS was far from the saturation regime, which agrees with the steep rise in SRS with laser intensity (i.e., SRS increased by 2.3 times with a 10 % increase in laser intensity). However, laser intensity was well above the threshold of convective TPD, and therefore it occurred in the saturation regimes as the $\omega_0/2$ intensity remained virtually the same with increasing laser intensity. This also explains why the TPD signal was observed earlier than SRS in the time-resolved optical spectrometer, as shown in Fig. 4.7. Since the gain of TPD is high, TPD was observed in early timing even when laser intensity was still low. These discussions indicate that TPD was dominant in this experimental condition, and therefore HE should be produced mainly by TPD. This can be further verified by comparing SRS reflectivity and HE conversion ratio. For example, in SN 44681, SRS reflectivity was 0.03 %, while HE conversion ratio was evaluated 0.3 % in the shot from the HEXS. One order magnitude smaller SRS reflectivity indicates that SRS is not a main mechanism for HE generation in this condition. It should be noted that this discussion is consistent with Gabriele *et al.* referring experimental data at GEKKO-XII under similar experimental conditions [109].

4.6. SRS, TPD, and hot electrons in diamond targets (Hydrogen effects in ablator material)

4.6.1. Experimental data

Here, SRS, TPD, and HEs in diamond target were explored, and compared to plastic targets. For direct comparison of C and CH_2 targets, the two shots for the same laser conditions are mainly compared here. Fig. 4.26 shows the time-integrated backscattered spectra measured for SN 44681 (CH_2) and SN 44685 (C). The shapes of the spectra are similar, indicating broad peak emissions at ~580 nm emitted by convective SRS (n_e~$0.13n_c$) and at ~690 nm due to convective TPD (n_e~$0.23n_c$). However, the spectrally integrated intensity of SRS light (λ=560–640 nm) for the shot on the CH_2 target was 14 times greater than that obtained on the C target, whereas the ratio of the integrated intensities of $\omega_0/2$ (λ=650–700 nm) was reduced to five. Correspondingly, the Cu-Kα intensity from the X-ray spectrometer suggests that the HE fluence in the CH_2 target was 4 times greater than that in the C target. Note that the different HE stopping and X-ray radiation powers in different ablator materials were corrected using PHITS simulation, assuming that single Maxwellian electron beam hits the targets that consist of C (3.5 g/cm^3 40 μm) and CH_2 (0.96 g/cm^3 10 μm) with a 25 μm Cu layer. Here, the HEXS signals in the C targets were overly low to allow a reliable analysis to compare the results of the CH_2 target presented above. Again, the increase in HEs can be explained by enhanced TPD.

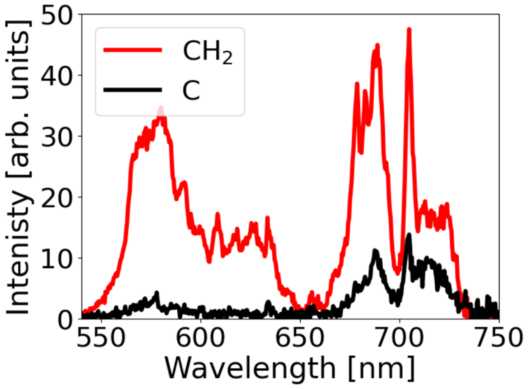

Figure 4.26. Backscattered lights from time-integrated optical spectrometer for C and CH_2.

4.6.2. Discussion

The possible mechanisms responsible for the different enhancements in SRS and TPD between C and CH_2 targets are discussed. The Rosenbluth gain factors for convective SRS and TPD (G_{SRS} and G_{TPD}) were calculated based on the plasma parameters provided by the hydrosimulations. We obtained G_{SRS} of ~0.80 for both C and CH_2 targets at $0.13n_c$ at the peak laser time. G_{TPD} was 10.0 and 11.1 for C and CH_2, respectively, at $0.23n_c$ at 50 ps before peak laser time. It should be noted that the electron temperature was greater for the C plasma than for the CH_2 plasma owing to the higher collisional absorption (e.g., $T_{e,\,C}$=2.5 keV, $T_{e,\,CH2}$=2.2 keV at peak laser time), as shown in Fig. 4.25, although the density scale length was virtually the same. This led to a reduced TPD gain in the C plasma compared to that in the CH_2 plasma. Fig. 4.27 displays the plots of spectrally integrated intensity (a) for SRS and (b) for TPD versus laser intensity in all the pre-pulse irradiation shots and Fig. 4.27 (c) and (d) display the intensities versus the corresponding Rosenbluth gain factors.

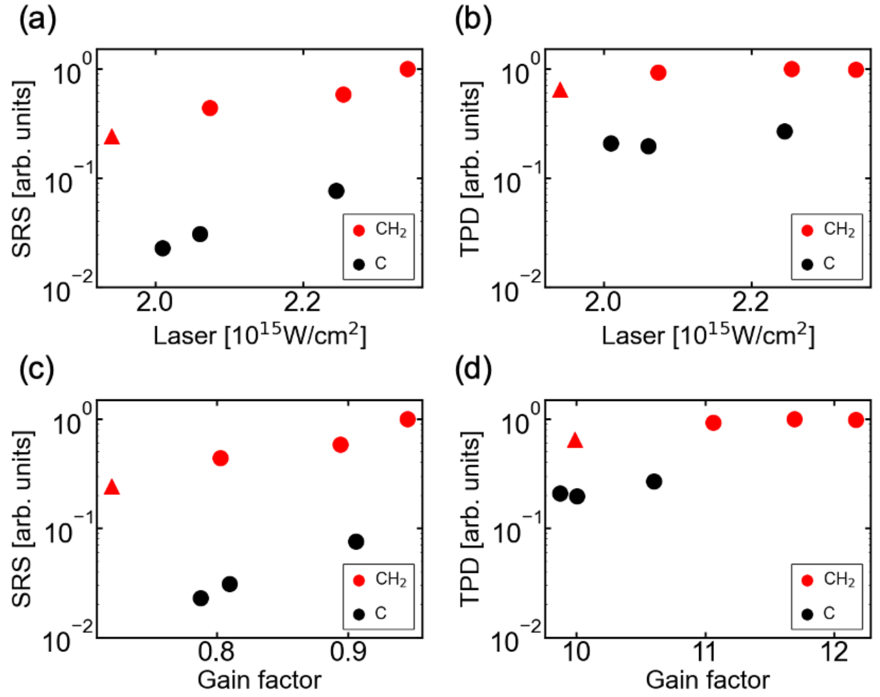

Figure 4.27. (a) Relationship between SRS and laser intensity. (b) Relationship between TPD and laser intensity. (c) Relationship between SRS and gain factor. (d) Relationship between TPD and gain factor. Note that the triangle plots refer to the CH target results.

Note that the error bars of the plots are within 10 %, smaller than the marker size, and the triangle plot refers to the result of a shot on a CH target. The results obtained for the CH and CH_2 targets were similar, which is discussed later in terms of the IAW damping. In TPD, a reasonable decrease in the gain factors for C was observed. However, as mentioned above, TPD was in a saturated regime, where its growth was only smoothly influenced by the difference in the expected gain, indicating a clear discrepancy in the saturation level between C and CH_2. Therefore, it is clear that the different extents of SRS and TPD between the C and CH_2 targets cannot be explained in terms of the Rosenbluth gain factors.

Damping of daughter waves reduces the growth of SRS and TPD to different extents for C and CH_2 plasmas, which could explain the experimental results. Williams *et al.* derived that the net gain factor of convective instability [110], accounting for the damping of the daughter waves, can be expressed by $G \cdot F(\Gamma)$, where the reduction factor:

$$F(\Gamma) = \frac{2}{\pi}\left(\arccos(\Gamma) - \Gamma\sqrt{1-\Gamma^2}\right) \tag{4.50}$$

Here, $\Gamma = \sqrt{\gamma_1\gamma_2}\,/\gamma_0$, and $\gamma_{1,2}$ depicts the damping rate of the daughter waves [110]. The damping rates of the EMW and LW were evaluated by considering collisions and the Landau effect as

$$\gamma_s = \frac{\nu_{ei}}{2}\frac{\omega_{pe}^2}{\omega_s^2} \tag{4.51}$$

$$\gamma_{LW} = \frac{\nu_{ei}}{2} + \nu_{ld} \tag{4.52}$$

where ω_{pe} and ω_s are the plasma and EMW frequencies, respectively, and ν_{ei} and ν_{ld} are collisional and Landau damping rates, respectively. Fig. 4.28 (a) and (b) display plots of the SRS and TPD integrated intensities versus the corresponding net gain values.

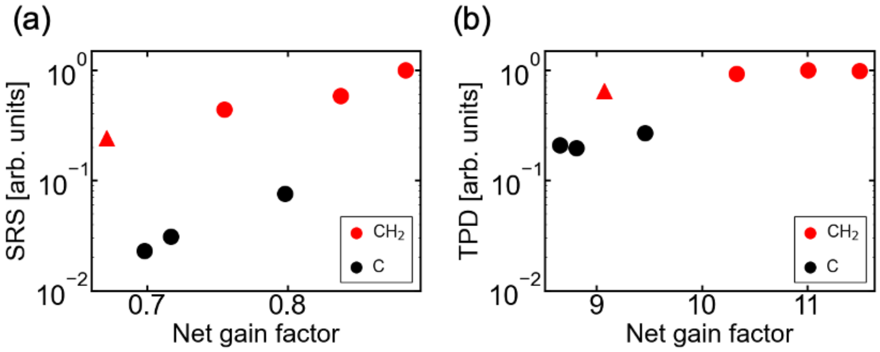

Figure 4.28. (a) Relationship between SRS and net gain factor. (b) Relationship between TPD and net gain factor. Note that the triangle plots refer to the CH target results.

As expected, the gain values became smaller than those obtained in the Rosenbluth gain, as indicated in Fig. 4.27 (c) and (d). However, the relative decrease in the net gains for the C and CH_2 targets remained overly small to explain the discrepancy observed in the SRS and $\omega_0/2$ intensities.

The above results suggest that additional mechanisms influenced by the presence of H in the ablator could have a role in determining the effective growth/saturation of both SRS and TPD. LDI is a possible saturation mechanism for SRS. In LDI, a LW decay into another LW and ion-acoustic wave (IAW), and therefore the occurrence of LDI saturates SRS [78–84,111,112]. In addition, kinetic effects such as phase shift, bowing, and self-focusing of LWs due to particle trapping have been suggested to cause SRS saturation [103–107,113,114]. Because such kinetic effects do not directly involve ion motion, here the effect of LDI was evaluated as a possible cause of the different extents of SRS. In addition, the $k\lambda_{De}$ values of the convective SRS in this experiment ($k\lambda_D$=0.28–0.19) indicate that such kinetic effects were not dominant because kinetic effects in convective SRS are typically observed in higher values of $k\lambda_{De} > 0.3$. The LDI threshold is described in terms of the density fluctuation [79].

$$\left(\frac{\delta n}{n_e}\right)_{LDI} = 4k\lambda_{De}\sqrt{\left(\frac{\nu_{IAW}}{\omega_{IAW}}\right)\left(\frac{\nu_{LW}}{\omega_{LW}}\right)} \tag{4.53}$$

where k, λ_{De}, ν, and ω are the LW wave number, Debye length, damping rate, and frequency, respectively. As demonstrated by this expression, a high IAW damping rate leads to a high LDI threshold, which results in favorable conditions for SRS, leading to a higher reflectivity level. Here, IAW damping rates were calculated at a plasma density of $0.13n_c$ from the plasma dielectric function: i.e., $1 + \chi_e + \sum_\beta \chi_{i\beta} = 0$, where χ_e and $\chi_{i\beta}$ denote the susceptibility of electrons and ions β, [115] obtaining $\nu_{IAW} / \omega_{IAW} = 0.007$ for C and 0.23 for CH_2. The LDI thresholds in terms of density fluctuation were calculated to be 0.006 and 0.022, respectively, reasonably verifying a lower reflectivity level of SRS in the C plasma with respect to the CH_2 plasma. It should also be noted that the ν_{IAW} / ω_{IAW} ratio for the CH plasma was 0.26; the difference with respect to CH_2 plasma was only 10 %, explaining the similar SRS intensities obtained for CH and CH_2 targets.

LDI is also a possible saturation mechanism in TPD [116,117]. However, a much smaller discrepancy of measured $\omega_0/2$ intensity for C and CH_2 plasma compared to that of SRS implies that other saturation mechanisms overwhelmed in the case of TPD. This is in agreement with previous simulation works, suggesting that TPD is saturated by ion density fluctuation and cavitation [92,118–122]. Weber *et al.* demonstrated the transition from LDI-induced saturation occurring at a low plasma temperature of ~0.5 keV to saturation by cavity and density fluctuation in plasmas at a temperature of 2 keV and greater, similar to our case [123]. In terms of IAW damping, Myatt *et al.* demonstrated, in the simulation, that the HE flux from TPD doubled with a 20 times increase in the IAW damping rate owing to a favorable nucleation-collapse-burnout cycle in cavitation, which was comparable to our results (four times enhanced HE by 30 times increased IAW damping) [124]. In addition, Seaton *et al.* suggested the same tendency [125]. The results obtained in this dissertation are the first experimental indication of the dependence of TPD on the IAW damping rate.

4.7. Summary and future prospects

LPIs are essential phenomena in ICF, and HEs generated by LPIs could be detrimental or beneficial in direct-drive ICF, depending on the design of implosion and the HE characteristics. In inhomogeneous plasma seen in direct-drive ICF conditions, the extent of SRS and TPD is typically described by Rosenbluth gain. However, other factors, such as the damping of plasma waves, could also affect their growth and saturation, and therefore, experimental investigation was required. This chapter first developed an experimental platform that enables the characterization of SRS, TPD, and HEs, and its consistency was confirmed through the cross-correlation of each diagnostic. The experimental results without pre-pulse and with pre-pulse shots for plastic targets showed that Rosenbluth gain could reasonably explain the experimental data. Also, from the experimental results of different laser intensities and the detailed discussion based on gain factors, it turned out that TPD occurred dominantly with high gain, mainly responsible for HE generation. In contrast, SRS occurred with low gain only in local high-intensity regions such as speckles. SRS, TPD, and HEs in diamond targets were also investigated and compared to plastic. The extent of SRS, TPD, and HEs decreased for diamond targets compared with plastic targets. Plasma inhomogeneity and different plasma temperatures could not explain the difference, and therefore, the greater extent in plastic targets was attributed to high IAW damping due to H ions. From the above, it was turned out that low H concentration is suitable to suppress HEs. Also, it is suggested that HEs could be controlled by H concentration in target materials. Regarding the target design, diamond capsules whose H concentration is as low as possible are ideal for convectional direct-drive ICF application because HEs cause fuel preheating. In SI scheme, the outer layer of the diamond capsule should also have the lowest H concentration to mitigate fuel preheating. On the other hand, HEs could have beneficial effects and should be actively controlled in the ignition phase when a spike pulse is launched. In this respect, H concentration in diamond in the deeper layer might have higher values to obtain HE fluence high enough to enhance ablation pressure. Further investigations are required to understand and model the effects of HEs on ablation pressure, which also would reveal an appropriate HE amount and energy. As a result, an ideal H concentration of ablator materials can be determined. For example, the diamond containing an H concentration of 4 at. % doubles the IAW damping rate compared with a pure carbon ablator. Here, it also should be noted that ~1 at. % H concentration in the diamond evaluated in Chapter 3 leads to ~20 % increase in the IAW damping rate, which could slightly increase SRS. H concentration in polycrystalline diamond deposited by CVD is known to be adjusted by deposition parameters up to ~10 at. %. Also, H concentration can be even higher in diamond-like carbon. In this respect, a two-layer capsule (First layer: the lowest H concentration/second layer: higher H concentration) might be suitable for the SI scheme application.

5. Conclusion

Nuclear fusion is an attractive energy source for the future, which can produce large amounts of fusion energy while not emitting any greenhouse gases, and the fuels are unexhausted. In ICF, a fuel capsule that contains fusion fuels is compressed by high-power lasers to create ultrahigh density and ultrahigh temperature states where fusion reactions can occur. ICF is promising because the repetition rate of the laser easily controls power production.

In direct-drive ICF, laser non-uniformity causes ablation surface perturbations called laser imprinting that is amplified by RT instability during implosion. Several target-based approaches were suggested to mitigate those issues, such as a foam target, a high Z coating, and a diamond target. Also, advanced schemes such as FI scheme and SI scheme were suggested, where the implosion is divided into the compression stage and the ignition stage. This study focused on diamond targets. Diamond is a low Z element, which is essential to avoid radiation, and it can mitigate laser imprinting thanks to low compressibility and higher density than conventional plastic targets. Moreover, it can be used with other techniques such as high Z coating, and it can be applied to advanced schemes such as SI scheme. This dissertation explored the fabrication of diamond capsules in a way that can apply to mass production required in future power plants. Also, LPIs and HEs were explored to obtain fundamental knowledge in diamond targets.

The fabrication process of diamond capsules by HF-CVD technique was proposed by Kato et al., which is advantageous for mass production because the deposition area can be extended only by increasing the number of filaments. This study improved the process of obtaining higher-quality diamond capsules. The deposition conditions were optimized regarding the vibration rate of the Mo stage and CH_4 concentration in source gases, and the etching process of the Si substrate was also modified to address the issues of Si residuals revealed in the preliminary laser experiment. Also, the fabricated diamond capsules were comprehensively characterized in terms of thickness, density, surface roughness, non-diamond contents, and mode amplitudes. As a result, it was shown that deposition duration could control thickness, density was 3.2 g/cm^3 (lower than single crystal diamond 3.5 g/cm^3), and the surface roughens were several 10 nm. It contained H (1.2 at. %), W (0.017 at. %), and sp^2 (graphitic content) that reasonably explained the lower density of the deposited diamond. Then, diamond capsules were introduced into a laser irradiation experiment, and successful implosion was observed in X-ray streak cameras, an X-ray framing camera, and X-ray pinhole cameras. Implosion trajectories were also compared with radiation hydrodynamic simulation calculations, which showed reasonable agreement within the error bars. These results indicated that diamond capsules can be fabricated in a process that applies to mass production for future power generation, and these facts inspire further experimental works to improve the quality of diamond capsules in the future.

LPIs are essential phenomena in ICF, and HEs generated by LPIs could be detrimental or beneficial in direct-drive ICF, and understanding them is a prerequisite. In inhomogeneous plasma in direct-drive ICF conditions, the extent of SRS and TPD is typically described by Rosenbluth gain that considers damping due to plasma inhomogeneity. However, other saturation mechanisms, such as LW damping, could also affect their growth and saturation, and therefore, experimental investigation was required. In this study, an experimental platform that enables the characterization of SRS, TPD, and HEs was established, and its consistency was confirmed through the cross-correlation of each diagnostic. From the experimental results referring to plastic targets, it was found that the tendency of experimental data can be explained by Rosenbluth gain, and calculation of the gain factors revealed that TPD occurred dominantly with high gain values, mainly responsible for HE generation. In contrast, SRS occurred with low gain values only in local high-intensity regions such as laser speckles. SRS, TPD, and HEs in diamond targets were also explored compared to plastic targets, observing that SRS, TPD, and HEs decreased in diamond. The difference between diamond and plastic was attributed to high IAW damping due to H ions in plastic, which suggested that H concentration should be minimized to suppress HEs, whereas HEs could be controlled by H concentration in the ablator material in some applications. Therefore, in target design, diamond capsules whose H concentration is as small as possible are ideal for convectional direct-drive ICF application because HEs lead to fuel preheating. On the other hand, in the SI scheme where HEs should be avoided in the compression phase, whereas HEs could contribute to ablation pressure enhancement in the ignition phase, a layer-capsule (First layer: the lowest H concentration/ Second layer: higher H concentration) might be suitable.

References

[1] S. Atzeni and J. Meyer-ter-Vehn, *The Physics of Inertial Fusion: BeamPlasma Interaction, Hydrodynamics, Hot Dense Matter* (Oxford University Press, 2004).

[2] H.-S. Bosch and G. M. Hale, *Improved Formulas for Fusion Cross-Sections and Thermal Reactivities*, Nuclear Fusion **32**, 611 (1992).

[3] J. Nuckolls, L. Wood, A. Thiessen, and G. Zimmerman, *Laser Compression of Matter to Super-High Densities: Thermonuclear (CTR) Applications Pressure: Implosion, Ablation*, Nature **239**, 139 (1972).

[4] J. P. Freidberg, *Plasma Physics and Fusion Energy* (Cambridge University Press, 2007).

[5] H. Abu-Shawareb et al., *Lawson Criterion for Ignition Exceeded in an Inertial Fusion Experiment*, Phys Rev Lett **129**, 075001 (2022).

[6] A. L. Kritcher et al., *Design of an Inertial Fusion Experiment Exceeding the Lawson Criterion for Ignition*, Phys Rev E **106**, 025201 (2022).

[7] A. B. Zylstra et al., *Experimental Achievement and Signatures of Ignition at the National Ignition Facility*, Phys Rev E **106**, 025202 (2022).

[8] Y. Izawa, T. Norimatsu, and C. Yamanaka, *Target Fabrication Activities in Japan*, Journal of Vacuum Science & Technology A: Vacuum, Surfaces, and Films **3**, 1252 (1985).

[9] M. D. Rosen, *The Physics Issues That Determine Inertial Confinement Fusion Target Gain and Driver Requirements: A Tutorial*, Phys Plasmas **6**, 1690 (1999).

[10] 疇地宏, *レーザー核融合とレーザープラズマ応用の発展 1.1. レーザー核融合研究の概念*, プラズマ・核融合学会誌 **81**, 2 (2005).

[11] R. S. Craxton et al., *Direct-Drive Inertial Confinement Fusion: A Review*, Phys Plasmas **22**, 110501 (2015).

[12] C. Yamanaka et al., *Laser Implosion of High-Aspect-Ratio Targets Produces Thermonuclear Neutron Yields Exceeding 1012 by Use of Shock Multiplexing*, Phys Rev Lett **56**, 1575 (1986).

[13] 佐宗 章弘, 圧縮性流体力学・衝撃波 (コロナ社, 2017).

[14] W. M. Manheimer, D. G. Colombant, and J. H. Gardner, *Steady-State Planar Ablative Flow*, Phys Fluids **25**, 1644 (1982).

[15] B. Canaud, X. Fortin, F. Garaude, C. Meyer, F. Philippe, M. Temporal, S. Atzeni, and A. Schiavi, *High-Gain Direct-Drive Target Design for the Laser*

Mégajoule, Nuclear Fusion **44**, 1118 (2004).

[16] N. Fleurot, C. Cavailler, and J. L. Bourgade, *The Laser Mégajoule (LMJ) Project Dedicated to Inertial Confinement Fusion: Development and Construction Status*, Fusion Engineering and Design **74**, 147 (2005).

[17] W. Zheng et al., *Laser Performance of the SG-III Laser Facility*, High Power Laser Science and Engineering **4**, e21 (2016).

[18] K. Jungwirth et al., *The Prague Asterix Laser System*, Phys Plasmas **8**, 2495 (2001).

[19] T. R. Boehly et al., *Initial Performance Results of the OMEGA Laser System*, Opt Commun **133**, 495 (1997).

[20] G. H. Miller, *The National Ignition Facility*, Optical Engineering **43**, 2841 (2004).

[21] C. Yamanaka, Y. Kato, Y. Izawa, K. Yoshida, T. Yamanaka, T. Sasaki, M. Nakatsuka, T. Mochizuki, J. Kuroda, and S. Nakai, *Nd-Doped Phosphate Glass Laser Systems for Laser-Fusion Research*, IEEE J Quantum Electron **17**, 1639 (1981).

[22] K. Shigemori, H. Azechi, M. Nakai, M. Honda, K. Meguro, N. Miyanaga, H. Takabe, and K. Mima, *Measurements of Rayleigh-Taylor Growth Rate of Planar Targets Irradiated Directly by Partially Coherent Light*, Phys Rev Lett **78**, 250 (1997).

[23] J. D. Hager, T. J. B. Collins, V. A. Smalyuk, J. P. Knauer, D. D. Meyerhofer, and T. C. Sangster, *Study of Rayleigh–Taylor Growth in Laser Irradiated Planar* SiO_2 *Targets at Ignition-Relevant Conditions*, Phys Plasmas **20**, 072707 (2013).

[24] V. A. Smalyuk et al., *Hydrodynamic Instability Growth and Mix Experiments at the National Ignition Facility*, Phys Plasmas **21**, 056301 (2014).

[25] H. Takabe, K. Mima, L. Montierth, and R. L. Morse, *Self-Consistent Growth Rate of the Rayleigh–Taylor Instability in an Ablatively Accelerating Plasma*, Phys Fluids **28**, 3676 (1985).

[26] J. D. Kilkenny, S. G. Glendinning, S. W. Haan, B. A. Hammel, J. D. Lindl, D. Munro, B. A. Remington, S. V. Weber, J. P. Knauer, and C. P. Verdon, *A Review of the Ablative Stabilization of the Rayleigh–Taylor Instability in Regimes Relevant to Inertial Confinement Fusion*, Phys Plasmas **1**, 1379 (1994).

[27] Hiroki Kato, Formation of Spatial Perturbation on Diamond Foils Due to Nonuniform Laser Irradiation on Direct-Drive Inertial Confinement Fusion, Osaka University, 2018.

[28] K. Shigemori, H. Azechi, M. Nakai, T. Endo, T. Nagaya, and T. Yamanaka, *Perturbation Transfer from the Front to Rear Surface of Laser-Irradiated Targets*, Phys Rev E **65**, 045401 (2002).

[29] S. P. Regan et al., *Dependence of Shell Mix on Feedthrough in Direct Drive Inertial Confinement Fusion*, Phys Rev Lett **92**, 185002 (2004).

[30] Y. Kato, K. Mima, N. Miyanaga, S. Arinaga, Y. Kitagawa, M. Nakatsuka, and C. Yamanaka, *Random Phasing of High-Power Lasers for Uniform Target Acceleration and Plasma-Instability Suppression*, Phys Rev Lett **53**, 1057 (1984).

[31] S. N. Dixit, K. A. Nugent, J. K. Lawson, K. R. Manes, and H. T. Powell, *Kinoform Phase Plates for Focal Plane Irradiance Profile Control*, Opt Lett **19**, 417 (1994).

[32] R. H. Lehmberg and S. P. Obenschain, *Use of Induced Spatial Incoherence for Uniform Illumination of Laser Fusion Targets*, Opt Commun **46**, 27 (1983).

[33] S. Skupsky, R. W. Short, T. Kessler, R. S. Craxton, S. Letzring, and J. M. Soures, *Improved Laser-Beam Uniformity Using the Angular Dispersion of Frequency-Modulated Light*, J Appl Phys **66**, 3456 (1989).

[34] J. Lindl, *Development of the Indirect-Drive Approach to Inertial Confinement Fusion and the Target Physics Basis for Ignition and Gain*, Phys Plasmas **2**, 3933 (1995).

[35] Y. Mori et al., *1 Hz Fast-Heating Fusion Driver HAMA Pumped by a 10 J Green Diode-Pumped Solid-State Laser*, Nuclear Fusion **53**, 073011 (2013).

[36] M. H. Emery, J. H. Gardner, R. H. Lehmberg, and S. P. Obenschain, *Hydrodynamic Target Response to an Induced Spatial Incoherence-Smoothed Laser Beam*, Physics of Fluids B: Plasma Physics **3**, 2640 (1991).

[37] S. P. Obenschain et al., *Effects of Thin High-Z Layers on the Hydrodynamics of Laser-Accelerated Plastic Targets*, Phys Plasmas **9**, 2234 (2002).

[38] H. Kato, K. Shigemori, H. Nagatomo, M. Nakai, T. Sakaiya, T. Ueda, H. Terasaki, Y. Hironaka, K. Shimizu, and H. Azechi, *Effect of Equation of State on Laser Imprinting by Comparing Diamond and Polystyrene Foils*, Phys Plasmas **25**, 032706 (2018).

[39] M. Tabak, D. Hinkel, S. Atzeni, E. M. Campbell, and K. Tanaka, *Fast Ignition: Overview and Background*, Fusion Science and Technology **49**, 254 (2006).

[40] R. Betti, C. D. Zhou, K. S. Anderson, L. J. Perkins, W. Theobald, and A. A. Solodov, *Shock Ignition of Thermonuclear Fuel with High Areal Density*, Phys Rev Lett **98**, 155001 (2007).

[41] R. Kodama et al., *Fast Heating of Ultrahigh-Density Plasma as a Step towards Laser Fusion Ignition*, Nature **412**, 798 (2001).

[42] P. A. Norreys et al., *Experimental Studies of the Advanced Fast Ignitor Scheme*, Phys Plasmas **7**, 3721 (2000).

[43] X. Ribeyre, M. Lafon, G. Schurtz, M. Olazabal-Loumé, J. Breil, S. Galera, and S. Weber, *Shock Ignition: Modelling and Target Design Robustness*, Plasma Phys Control Fusion **51**, 124030 (2009).

[44] J. A. Delettrez, T. J. B. Collins, and C. Ye, *Determining Acceptable Limits of Fast-Electron Preheat in Direct-Drive-Ignition–Scale Target Designs*, Phys Plasmas **26**, 062705 (2019).

[45] R. E. Kidder, *Hot-Electron Preheat of Laser-Driven Targets*, Nuclear Fusion **21**, 145 (1981).

[46] S. Gus'kov, X. Ribeyre, M. Touati, J.-L. Feugeas, Ph. Nicolaï, and V. Tikhonchuk, *Ablation Pressure Driven by an Energetic Electron Beam in a Dense Plasma*, Phys Rev Lett **109**, 255004 (2012).

[47] D. Batani et al., *Physics Issues for Shock Ignition*, Nuclear Fusion **54**, 054009 (2014).

[48] R. Nora et al., *Gigabar Spherical Shock Generation on the OMEGA Laser*, Phys Rev Lett **114**, 045001 (2015).

[49] W. Theobald et al., *Enhanced Hot-Electron Production and Strong-Shock Generation in Hydrogen-Rich Ablators for Shock Ignition*, Phys Plasmas **24**, 120702 (2017).

[50] K. A. Brueckner and S. Jorna, *Laser-Driven Fusion*, Rev Mod Phys **46**, 325 (1974).

[51] K. Katagiri, N. Ozaki, Y. Umeda, T. Irifune, N. Kamimura, K. Miyanishi, T. Sano, T. Sekine, and R. Kodama, *Shock Response of Full Density Nanopolycrystalline Diamond*, Phys Rev Lett **125**, 185701 (2020).

[52] J. Biener et al., *Diamond Spheres for Inertial Confinement Fusion*, Nuclear Fusion **49**, 112001 (2009).

[53] J. S. Ross et al., *High-Density Carbon Capsule Experiments on the National Ignition Facility*, Phys Rev E **91**, 021101 (2015).

[54] A. J. MacKinnon et al., *High-Density Carbon Ablator Experiments on the National Ignition Facility*, Phys Plasmas **21**, 056318 (2014).

[55] W. Ding, J. Han, Q. Hu, Y. Chen, F. Liu, Y. Liu, L. Gou, D. He, and G. Zhan, *Stress Control of Heterogeneous Nanocrystalline Diamond Sphere through Pressure-Temperature Tuning*, Appl Phys Lett **110**, 121908 (2017).

[56] H. Kato, H. Yamada, S. Ohmagari, A. Chayahara, Y. Mokuno, Y. Fukuyama, N. Fujiwara, K. Miyanishi, Y. Hironaka, and K. Shigemori, *Synthesis and Characterization of Diamond Capsules for Direct-Drive Inertial Confinement Fusion*, Diam Relat Mater **86**, 15 (2018).

[57] S. Matsumoto, Y. Sato, M. Tsutsumi, and N. Setaka, *Growth of Diamond Particles from Methane-Hydrogen Gas*, J Mater Sci **17**, 3106 (1982).

[58] E. M. A. Fuentes-Fernandez et al., *Synthesis and Characterization of Microcrystalline Diamond to Ultrananocrystalline Diamond Films via Hot Filament Chemical Vapor Deposition for Scaling to Large Area Applications*, Thin Solid Films **603**, 62 (2016).

[59] L. C. Nistor, J. Van Landuyt, V. G. Ralchenko, E. D. Obraztsova, and A. A. Smolin, *Nanocrystalline Diamond Films: Transmission Electron Microscopy and Raman Spectroscopy Characterization*, Diam Relat Mater **6**, 159 (1997).

[60] S. Prawer, K. W. Nugent, D. N. Jamieson, J. O. Orwa, L. A. Bursill, and J. L. Peng, *The Raman Spectrum of Nanocrystalline Diamond*, Chem Phys Lett **332**, 93 (2000).

[61] D. Ballutaud, F. Jomard, T. Kociniewski, E. Rzepka, H. Girard, and S. Saada, *Sp3/Sp2 Character of the Carbon and Hydrogen Configuration in Micro- and Nanocrystalline Diamond*, Diam Relat Mater **17**, 451 (2008).

[62] K. M. McNamara, K. K. Gleason, D. J. Vestyck, and J. E. Butler, *Evaluation of Diamond Films by Nuclear Magnetic Resonance and Raman Spectroscopy*, Diam Relat Mater **1**, 1145 (1992).

[63] C. Dawedeit et al., *Grain Size Dependent Physical and Chemical Properties of Thick CVD Diamond Films for High Energy Density Physics Experiments*, Diam Relat Mater **40**, 75 (2013).

[64] J. Robertson, *Diamond-like Amorphous Carbon*, Materials Science and Engineering: R: Reports **37**, 129 (2002).

[65] N. Wada and S. A. Solin, *Raman Efficiency Measurements of Graphite*, Physica B+C **105**, 353 (1981).

[66] R. Pfeiffer, H. Kuzmany, N. Salk, and B. Günther, *Evidence for Trans-Polyacetylene in Nanocrystalline Diamond Films from H–D Isotropic Substitution Experiments*, Appl Phys Lett **82**, 4149 (2003).

[67] A. C. Ferrari and J. Robertson, *Origin of the 1150−cm−1 Raman Mode in Nanocrystalline Diamond*, Phys Rev B **63**, 121405 (2001).

[68] M. Itoh, K. Sato, and T. Kuboi, *Diameter Measurements System of Solder Ball*, Hitachi Metals Technical Review **19**, (2003).

[69] S. W. Haan, T. Dittrich, G. Strobel, S. Hatchett, D. Hinkel, M. Marinak, D. Munro, O. Jones, S. Pollaine, and L. Suter, *Update on Ignition Target Fabrication Specifications*, Fusion Science and Technology **41**, 164 (2002).

[70] H. Takabe et al., *Scalings of Implosion Experiments for High Neutron Yield*, Phys Fluids **31**, 2884 (1988).

[71] H. Nagatomo, T. Johzaki, T. Nakamura, H. Sakagami, A. Sunahara, and K. Mima, *Simulation and Design Study of Cryogenic Cone Shell Target for Fast Ignition Realization Experiment Project*, Phys Plasmas **14**, 056303 (2007).

[72] W. L. Kruer, *The Physics Of Laser Plasma Interactions* (CRC Press, Boca Raton, 2019).

[73] S. Pfalzner, *An Introduction to Inertial Confinement Fusion* (CRC Press, 2006).

[74] F. F. Chen, *Introduction to Plasma Physics* (Springer US, Boston, MA, 1995).

[75] M. N. Rosenbluth, *Parametric Instabilities in Inhomogeneous Media*, Phys Rev Lett **29**, 565 (1972).

[76] C. S. Liu, M. N. Rosenbluth, and R. B. White, *Raman and Brillouin Scattering of Electromagnetic Waves in Inhomogeneous Plasmas*, Phys Fluids **17**, 1211 (1974).

[77] C. Z. Xiao, Z. J. Liu, C. Y. Zheng, and X. T. He, *Competition between Stimulated Raman Scattering and Two-Plasmon Decay in Inhomogeneous Plasma*, Phys Plasmas **23**, 022704 (2016).

[78] S. Depierreux, J. Fuchs, C. Labaune, A. Michard, H. A. Baldis, D. Pesme, S. Hüller, and G. Laval, *First Observation of Ion Acoustic Waves Produced by the Langmuir Decay Instability*, Phys Rev Lett **84**, 2869 (2000).

[79] R. K. Kirkwood et al., *Effect of Ion-Wave Damping on Stimulated Raman Scattering in High-Z Laser-Produced Plasmas*, Phys Rev Lett **77**, 2706 (1996).

[80] C. Labaune, H. A. Baldis, B. S. Bauer, V. T. Tikhonchuk, and G. Laval, *Time-Resolved Measurements of Secondary Langmuir Waves Produced by the Langmuir Decay Instability in a Laser-Produced Plasma*, Phys Plasmas **5**, 234 (1998).

[81] T. Kolber, W. Rozmus, and V. T. Tikhonchuk, *Saturation of Stimulated Raman Scattering by Langmuir and Ion-acoustic Wave Coupling*, Physics of Fluids B: Plasma Physics **5**, 138 (1993).

[82] D. T. Michel, S. Depierreux, C. Stenz, V. Tassin, and C. Labaune, *Exploring the Saturation Levels of Stimulated Raman Scattering in the Absolute Regime*, Phys Rev Lett **104**, 255001 (2010).

[83] S. Depierreux, C. Labaune, J. Fuchs, D. Pesme, V. T. Tikhonchuk, and H. A.

Baldis, *Langmuir Decay Instability Cascade in Laser-Plasma Experiments*, Phys Rev Lett **89**, 045001 (2002).

[84] J. C. Fernández, J. A. Cobble, B. H. Failor, D. F. DuBois, D. S. Montgomery, H. A. Rose, H. X. Vu, B. H. Wilde, M. D. Wilke, and R. E. Chrien, *Observed Dependence of Stimulated Raman Scattering on Ion-Acoustic Damping in Hohlraum Plasmas*, Phys Rev Lett **77**, 2702 (1996).

[85] R. M. Stevenson et al., *Effects of Plasma Composition on Backscatter, Hot Electron Production, and Propagation in Underdense Plasmas*, Phys Plasmas **11**, 2709 (2004).

[86] J. R. Fein et al., *Mitigation of Hot Electrons from Laser-Plasma Instabilities in High-Z, Highly Ionized Plasmas*, Phys Plasmas **24**, 032707 (2017).

[87] R. K. Follett et al., *Two-Plasmon Decay Mitigation in Direct-Drive Inertial-Confinement-Fusion Experiments Using Multilayer Targets*, Phys Rev Lett **116**, 155002 (2016).

[88] W. Seka, B. B. Afeyan, R. Boni, L. M. Goldman, R. W. Short, K. Tanaka, and T. W. Johnston, *Diagnostic Value of Odd-Integer Half-Harmonic Emission from Laser-Produced Plasmas*, Physics of Fluids **28**, 2570 (1985).

[89] I. H. Malitson, *Interspecimen Comparison of the Refractive Index of Fused Silica*,†*, J Opt Soc Am **55**, 1205 (1965).

[90] G. Cristoforetti et al., *Measurements of Parametric Instabilities at Laser Intensities Relevant to Strong Shock Generation*, Phys Plasmas **25**, 012702 (2018).

[91] G. Cristoforetti et al., *Time Evolution of Stimulated Raman Scattering and Two-Plasmon Decay at Laser Intensities Relevant for Shock Ignition in a Hot Plasma*, High Power Laser Science and Engineering **7**, e51 (2019).

[92] R. Yan, A. V. Maximov, C. Ren, and F. S. Tsung, *Growth and Saturation of Convective Modes of the Two-Plasmon Decay Instability in Inertial Confinement Fusion*, Phys Rev Lett **103**, 175002 (2009).

[93] S. Masuda, E. Miura, K. Koyama, and S. Kato, *Absolute Calibration of an Electron Spectrometer Using High Energy Electrons Produced by the Laser-Plasma Interaction*, Review of Scientific Instruments **79**, 083301 (2008).

[94] A. L. Meadowcroft, C. D. Bentley, and E. N. Stott, *Evaluation of the Sensitivity and Fading Characteristics of an Image Plate System for X-Ray Diagnostics*, Review of Scientific Instruments **79**, 113102 (2008).

[95] S. Kojima et al., *Electromagnetic Field Growth Triggering Super-Ponderomotive Electron Acceleration during Multi-Picosecond Laser-Plasma*

Interaction, Commun Phys **2**, 99 (2019).

[96] C. D. Chen et al., *A Bremsstrahlung Spectrometer Using K-Edge and Differential Filters with Image Plate Dosimeters*, Review of Scientific Instruments **79**, 10E305 (2008).

[97] P. Koester et al., *Bremsstrahlung Cannon Design for Shock Ignition Relevant Regime*, Review of Scientific Instruments **92**, 013501 (2021).

[98] T. Sato et al., *Features of Particle and Heavy Ion Transport Code System (PHITS) Version 3.02*, J Nucl Sci Technol **55**, 684 (2018).

[99] J. E. Miller, T. R. Boehly, A. Melchior, D. D. Meyerhofer, P. M. Celliers, J. H. Eggert, D. G. Hicks, C. M. Sorce, J. A. Oertel, and P. M. Emmel, *Streaked Optical Pyrometer System for Laser-Driven Shock-Wave Experiments on OMEGA*, Review of Scientific Instruments **78**, 034903 (2007).

[100] D. G. Hicks, T. R. Boehly, P. M. Celliers, J. H. Eggert, E. Vianello, D. D. Meyerhofer, and G. W. Collins, *Shock Compression of Quartz in the High-Pressure Fluid Regime*, Phys Plasmas **12**, 082702 (2005).

[101] P. M. Celliers, P. Loubeyre, J. H. Eggert, S. Brygoo, R. S. McWilliams, D. G. Hicks, T. R. Boehly, R. Jeanloz, and G. W. Collins, *Insulator-to-Conducting Transition in Dense Fluid Helium*, Phys Rev Lett **104**, 184503 (2010).

[102] P. M. Celliers, D. K. Bradley, G. W. Collins, D. G. Hicks, T. R. Boehly, and W. J. Armstrong, *Line-Imaging Velocimeter for Shock Diagnostics at the OMEGA Laser Facility*, Review of Scientific Instruments **75**, 4916 (2004).

[103] H. X. Vu, D. F. DuBois, and B. Bezzerides, *Transient Enhancement and Detuning of Laser-Driven Parametric Instabilities by Particle Trapping*, Phys Rev Lett **86**, 4306 (2001).

[104] D. S. Montgomery, J. A. Cobble, J. C. Fernández, R. J. Focia, R. P. Johnson, N. Renard-LeGalloudec, H. A. Rose, and D. A. Russell, *Recent Trident Single Hot Spot Experiments: Evidence for Kinetic Effects, and Observation of Langmuir Decay Instability Cascade*, Phys Plasmas **9**, 2311 (2002).

[105] L. Yin, B. J. Albright, K. J. Bowers, W. Daughton, and H. A. Rose, *Saturation of Backward Stimulated Scattering of a Laser Beam in the Kinetic Regime*, Phys Rev Lett **99**, 265004 (2007).

[106] S. J. Spencer, A. G. Seaton, T. Goffrey, and T. D. Arber, *Inflationary Stimulated Raman Scattering in Shock-Ignition Plasmas*, Phys Plasmas **27**, 122705 (2020).

[107] D. Bénisti, O. Morice, L. Gremillet, E. Siminos, and D. J. Strozzi, *Self-Organization and Threshold of Stimulated Raman Scattering*, Phys Rev Lett

105, 015001 (2010).

[108] J. Garnier, *Statistics of the Hot Spots of Smoothed Beams Produced by Random Phase Plates Revisited*, Phys Plasmas **6**, 1601 (1999).

[109] G. Cristoforetti et al., *Multibeam Laser Plasma Interaction at Gekko XII Laser Facility in Conditions Relevant for Direct-Drive Inertial Confinement Fusion*, High Power Laser Science and Engineering **11**, e24 (2023).

[110] E. A. Williams, *Convective Growth of Parametrically Unstable Modes in Inhomogeneous Media*, Physics of Fluids B: Plasma Physics **3**, 1504 (1991).

[111] D. S. Montgomery et al., *Evidence of Plasma Fluctuations and Their Effect on the Growth of Stimulated Brillouin and Stimulated Raman Scattering in Laser Plasmas*, Phys Plasmas **5**, 1973 (1998).

[112] R. K. Kirkwood, R. L. Berger, C. G. R. Geddes, J. D. Moody, B. J. MacGowan, S. H. Glenzer, K. G. Estabrook, C. Decker, and O. L. Landen, *Scaling of Saturated Stimulated Raman Scattering with Temperature and Intensity in Ignition Scale Plasmas*, Phys Plasmas **10**, 2948 (2003).

[113] L. Yin, W. Daughton, B. J. Albright, B. Bezzerides, D. F. DuBois, J. M. Kindel, and H. X. Vu, *Nonlinear Development of Stimulated Raman Scattering from Electrostatic Modes Excited by Self-Consistent Non-Maxwellian Velocity Distributions*, Phys Rev E **73**, 025401 (2006).

[114] A. Friou, D. Bénisti, L. Gremillet, E. Lefebvre, O. Morice, E. Siminos, and D. J. Strozzi, *Saturation Mechanisms of Backward Stimulated Raman Scattering in a One-Dimensional Geometry*, Phys Plasmas **20**, 103103 (2013).

[115] Q. S. Feng, C. Y. Zheng, Z. J. Liu, C. Z. Xiao, Q. Wang, and X. T. He, *Excitation of Nonlinear Ion Acoustic Waves in CH Plasmas*, Phys Plasmas **23**, 082106 (2016).

[116] H. X. Vu, D. F. DuBois, D. A. Russell, and J. F. Myatt, *The Reduced-Description Particle-in-Cell Model for the Two Plasmon Decay Instability*, Phys Plasmas **17**, 072701 (2010).

[117] R. K. Follett, D. H. Edgell, R. J. Henchen, S. X. Hu, J. Katz, D. T. Michel, J. F. Myatt, J. Shaw, and D. H. Froula, *Direct Observation of the Two-Plasmon-Decay Common Plasma Wave Using Ultraviolet Thomson Scattering*, Phys Rev E **91**, 031104 (2015).

[118] A. B. Langdon, B. F. Lasinski, and W. L. Kruer, *Nonlinear Saturation and Recurrence of the Two-Plasmon Decay Instability*, Phys Rev Lett **43**, 133 (1979).

[119] S. Weber, C. Riconda, O. Klimo, A. Héron, and V. T. Tikhonchuk, *Fast*

Saturation of the Two-Plasmon-Decay Instability for Shock-Ignition Conditions, Phys Rev E **85**, 016403 (2012).

[120] G. D. Doolen, D. F. Dubois, and H. A. Rose, *Nucleation of Cavitons in Strong Langmuir Turbulence*, Phys Rev Lett **54**, 804 (1985).

[121] D. Russell, D. F. DuBois, and H. A. Rose, *Nucleation in Two-Dimensional Langmuir Turbulence*, Phys Rev Lett **60**, 581 (1988).

[122] C. Riconda, S. Weber, V. T. Tikhonchuk, and A. Héron, *Kinetic Simulations of Stimulated Raman Backscattering and Related Processes for the Shock-Ignition Approach to Inertial Confinement Fusion*, Phys Plasmas **18**, 092701 (2011).

[123] S. Weber and C. Riconda, *Temperature Dependence of Parametric Instabilities in the Context of the Shock-Ignition Approach to Inertial Confinement Fusion*, High Power Laser Science and Engineering **3**, e6 (2015).

[124] J. F. Myatt, H. X. Vu, D. F. DuBois, D. A. Russell, J. Zhang, R. W. Short, and A. V. Maximov, *Mitigation of Two-Plasmon Decay in Direct-Drive Inertial Confinement Fusion through the Manipulation of Ion-Acoustic and Langmuir Wave Damping*, Phys Plasmas **20**, 052705 (2013).

[125] A. G. Seaton and T. D. Arber, *Laser-Plasma Instabilities in Long Scale-Length Plasmas Relevant to Shock-Ignition*, Phys Plasmas **27**, 082704 (2020).

Publications

First author

1. K. Kawasaki et al., *The Role of Hot Electrons on Ultrahigh Pressure Generation Relevant to Shock Ignition Conditions*, High Energy Density Phys **37**, 100892 (2020).
2. K. Kawasaki et al., *Direct-Drive Implosion Experiment of Diamond Capsules Fabricated with Hot Filament Chemical Vapor Deposition Technique*, Phys Plasmas **28**, 104501 (2021).
3. K. Kawasaki et al., *Fabrication of Nanocrystalline Diamond Capsules by Hot-Filament Chemical Vapor Deposition for Direct-Drive Inertial Confinement Fusion Experiments*, Diam Relat Mater **135**, 109896 (2023).
4. K. Kawasaki et al., *Effects of Hydrogen Concentration in Ablator Material on Stimulated Raman Scattering, Two-Plasmon Decay, and Hot Electrons for Direct-Drive Inertial Confinement Fusion*, Phys Rev Res **5**, 033051 (2023).

Co-author

1. Y. Maeda et al., *Observation of Ultra-High Energy Density State with x-Ray Free Electron Laser SACLA*, High Energy Density Phys **36**, 100813 (2020).
2. T. Iwasaki, K. Kawasaki, H. Yamada, S. Ohmagari, D. Takeuchi, A. Chayahara, Y. Mokuno, Y. Hironaka, and K. Shigemori, *Dependences of Morphology and Surface Roughness on Growth Conditions of Diamond Capsules for the Direct-Drive Inertial Confinement Fusion*, High Energy Density Phys **37**, 100849 (2020).
3. D. Mancelli et al., *Shock Hugoniot Data for Water up to 5 Mbar Obtained with Quartz Standard at High-Energy Laser Facilities*, Laser and Particle Beams **2021**, 1 (2021).
4. T. Tamagawa et al., *Development of an Experimental Platform for the Investigation of Laser–Plasma Interaction in Conditions Relevant to Shock Ignition Regime*, Review of Scientific Instruments **93**, 063505 (2022).
5. G. Cristoforetti et al., *Multibeam Laser–Plasma Interaction at the Gekko XII Laser Facility in Conditions Relevant for Direct-Drive Inertial Confinement Fusion*, High Power Laser Science and Engineering **11**, e24 (2023).
6. H. Sawada et al., *Ultrafast Time-Resolved 2D Imaging of Laser-Driven Fast Electron Transport in Solid Density Matter Using an x-Ray Free Electron Laser*, Review of Scientific Instruments **94**, 033511 (2023).
7. D. Tanaka et al., *Ultrahigh-Energy Density State in Nanowire Arrays Irradiated with Picosecond Kilojoule-Class Ultra-Intense Laser*, AIP Adv **13**, 125118 (2023).

Appendix

Determination of constant A in the SOP

The calibration experiments were performed to derive a value of constant *A* of the SOP system. In the calibration shot, in addition to the SOP, A VISAR was employed to measure shock wave velocity. A principle of the VISAR is based on a Doppler shift of surface movement and interferometry. When a shock wave propagates in the Qz layer, the reflectivity of Qz dramatically increases due to metallization. In the VISAR system, the laser is injected into the target from the back side of the target (Qz), and the reflected laser light is split into two passes, as shown in Fig. A1.

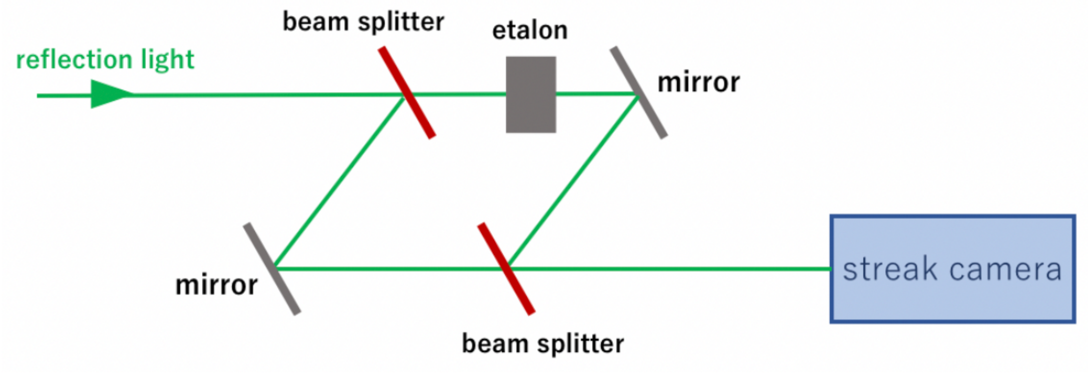

Figure. A1. Optical pass of the VISAR system.

The phase difference is created by inserting etalon into one pass, creating an interference fringe pattern. When a shock wave propagates in the Qz layer, due to the Doppler effect of the moving shock front, the phase difference varies from the stationary case, shown in Fig. A2. Here, the phase shift of the fringe pattern represents shock velocity by

$$v(\phi) = \phi\left[\frac{\lambda}{2\tau(1+\delta)}\right] \qquad (A1)$$

Where ϕ is a phase shift, and τ and δ are constant, that should be calculated depending on the setting of etalon. The term $\lambda/2\tau(1+\delta)$ is called velocity per fringe (VPF). Here, two VISARs were employed, and the VPF values were 5.554 km/s for VISAR1 and 9.024 km/s for VISAR2. For determining A, VISAR1 was employed. The streaked image of VISAR1 is shown in Fig. A2.

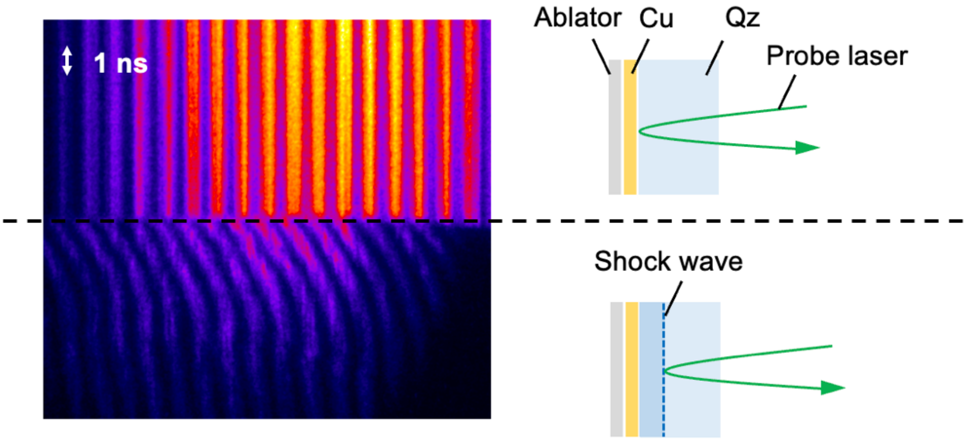

A2. Streaked image of VISAR1 and corresponding schematic image of shock propagation and laser light reflection.

The phase difference can be evaluated by performing a Fourier transformation of the image. From the phase shift from the stationary case, the shock velocity was evaluated as a function of time. It should be noted that shock velocity should be corrected by considering the reflective index of the Qz. In this experiment, the velocity jump was more than VPF. Therefore, candidates of shock velocity are infinite (i.e., $v_1 + i \times VPF1$). To find out appropriate i, VISAR2 was also analyzed, obtaining $v_2 + j \times VPF2$. i is determined by $v_1 + i \times VPF1 \sim v_2 + j \times VPF2$. Also, from the shock transit time in the Qz layer, the value of shock velocity was verified. From the above, shock velocity was evaluated as a function of time, and the shock velocity was converted to the shocked temperature. In the SOP, an emission intensity was obtained as a function of time. By comparing shocked temperature data from the VISAR1 and emission intensity data from the SOP in Eq. 4.47, the constant A was evaluated to 890 ± 290.